

Scaling of plate-tectonic convection with pseudoplastic rheology

Jun Korenaga

Department of Geology and Geophysics, Yale University, New Haven, CT

arXiv:1008.4782v1 [physics.geo-ph] 27 Aug 2010

¹ Short title: SCALING OF PLATE TECTONICS

2 **Abstract.** The scaling of plate-tectonic convection is investigated by simulating thermal
3 convection with pseudoplastic rheology and strongly temperature-dependent viscosity. The
4 effect of mantle melting is also explored with additional depth-dependent viscosity. Heat-flow
5 scaling can be constructed with only two parameters, the internal Rayleigh number and
6 the lithospheric viscosity contrast, the latter of which is determined entirely by rheological
7 properties. The critical viscosity contrast for the transition between plate-tectonic and
8 stagnant-lid convection is found to be proportional to the square root of the internal Rayleigh
9 number. The relation between mantle temperature and surface heat flux on Earth is discussed
10 on the basis of these scaling laws, and the inverse relationship between them, as previously
11 suggested from the consideration of global energy balance, is confirmed by this fully dynamic
12 approach. In the presence of surface water to reduce the effective friction coefficient, the
13 operation of plate tectonics is suggested to be plausible throughout the Earth history.

1. Introduction

Simulating mantle convection with plate tectonics in a fully dynamic manner has become popular in the last decade or so [e.g., *Bercovici*, 2003], and quite a few studies have been published addressing a variety of problems, including the significance of 3-D spherical geometry [*Richards et al.*, 2001; *van Heck and Tackley*, 2008; *Foley and Becker*, 2009], the role of history-dependent rheology [e.g., *Tackley*, 2000; *Ogawa*, 2003; *Landuyt et al.*, 2008], the initiation of subduction [*Solomatov*, 2004; *Gurnis et al.*, 2004], and applications to other terrestrial planets [e.g., *Lenardic et al.*, 2004; *O'Neill and Lenardic*, 2007; *Landuyt and Bercovici*, 2009]. Around the same time, interests in the initiation and evolution of plate tectonics over the Earth history have grown considerably [e.g., *Mojzsis et al.*, 2001; *Bleeker*, 2003; *Harrison et al.*, 2005; *Stern*, 2005; *Korenaga*, 2006; *Van Kranendonk et al.*, 2007; *O'Neill et al.*, 2007; *Condie and Pease*, 2008; *Bradley*, 2008; *Harrison*, 2009; *Herzberg et al.*, 2010]. Many of previous numerical studies on plate-tectonic convection are, however, exploratory in nature, and scaling laws relevant to such geological questions are yet to be established. Given the lack of consensus on why plate tectonics can take place on Earth to begin with [e.g., *Moresi and Solomatov*, 1998; *Gurnis et al.*, 2000; *Bercovici and Karato*, 2003; *Korenaga*, 2007], it may be premature to discuss the scaling of plate-tectonic convection, but it is nonetheless important to seek a strategy to bridge geology and geodynamics by taking into account peculiar complications associated with plate tectonics.

In this study, I attempt to derive the scaling of plate-tectonic convection using the so-called pseudoplastic rheology [*Moresi and Solomatov*, 1998], in which the strength of plates is controlled by temperature-dependent viscosity as well as brittle failure. It is known that, for this approach to be successful, the friction coefficient for brittle deformation has to be at least one order of magnitude lower than suggested by laboratory experiments. The presence of pore fluid deep in the oceanic lithosphere is required to explain such low friction, and because oceanic lithosphere is likely to be very dry upon its formation by melting under mid-ocean ridges [*Hirth and Kohlstedt*, 1996; *Evans et al.*, 2005], it may appear to be difficult to justify the pseudoplastic approach. The upper half of oceanic lithosphere, however, can

42 be pervasively fractured by thermal cracking, and in the presence of surface water, the deep
43 hydration of oceanic lithosphere is possible [Korenaga, 2007]. In this mechanism, the strong
44 temperature dependency of mantle rheology actually enhances thermal cracking. Another
45 concern with the pseudoplastic rheology is that it is determined only by the instantaneous
46 stress state and does not have any memory to simulate preexisting weakness, though this
47 limitation is not as grave as it may appear. With the thermal cracking hypothesis, the stiffest
48 part of oceanic lithosphere is continually damaged as it ages, so preexisting weakness is
49 globally distributed. Also, whatever the actual weakening mechanism would be, oceanic
50 lithosphere is eventually subducted (on the time scale of 100 Myr), and its memory of
51 weakness would keep being lost in the deep mantle. For the evolution of oceanic lithosphere,
52 therefore, the difference between instantaneous rheology and history-dependent rheology is
53 not expected to be vital [Tackley, 2000]. In plate tectonics, convective heat loss is dominated
54 by that from oceanic plates, so even with simple pseudoplastic rheology, we may still hope to
55 capture the gross characteristics of mantle convection relevant to the long-term evolution of
56 Earth.

57 The purpose of this paper is two-fold. First, I will investigate the scaling of plate-tectonic
58 convection with ‘standard’ pseudoplastic rheology, which is controlled by friction-based
59 yield stress and temperature-dependent viscosity. Though there exist a number of numerical
60 studies using this rheology, the temperature dependency of mantle viscosity is fairly weak in
61 most of these studies [e.g., Moresi and Solomatov, 1998; Lenardic et al., 2004; Stein et al.,
62 2004; O’Neill and Lenardic, 2007]; the maximum viscosity variation due to temperature
63 dependency is usually 10^6 . This may not seem to be low because it is high enough to put
64 convection in the stagnant-lid regime without pseudoplastic rheology. In basally-heated
65 convection, which is commonly adopted by those previous studies, there is an important
66 difference regarding thermal structure between stagnant-lid convection and plate-tectonic
67 convection. In the stagnant-lid regime, most of temperature variations are taken up by the
68 top thermal boundary layer, so viscosity variation across the top boundary layer is close to
69 the maximum viscosity variation employed. In the plate-tectonic regime with basal heating,
70 the top and bottom thermal boundary layers have similar temperature contrasts, i.e., the

71 temperature contrast across the top boundary layer (or plates) is basically halved, with the
 72 corresponding viscosity variation of only 10^3 . As explained in more detail later (§2.1), the
 73 viscosity contrast across oceanic lithosphere due to temperature dependency is expected to be
 74 at least $\exp(20) \sim 5 \times 10^8$. It is important to use strongly temperature-dependent viscosity so
 75 that we can discuss the scaling of plate-tectonic convection with more confidence. The second
 76 objective of this paper is to discuss the effects of mantle melting by adding depth-dependent
 77 viscosity to the standard pseudoplastic rheology. How mantle melting could modify the
 78 scaling of plate tectonics has important implications for the thermal evolution of Earth
 79 [Korenaga, 2003, 2006], but this issue has not been quantified by fully dynamic calculations.

80 This paper is organized as follows. After describing the details of theoretical formulation
 81 (§2), I will present numerical results, together with scaling analysis to understand the
 82 systematics of model behavior (§3). In the discussion section (§4), I will briefly explore how
 83 new scaling laws may be used to infer when plate tectonics initiated on Earth and how it
 84 evolved subsequently. Critiques on previous attempts to derive the scaling of plate tectonics
 85 are also provided.

86 2. Theoretical Formulation

87 2.1. Mantle Rheology

88 For temperature-dependent viscosity, I employ the following linear-exponential form:

$$89 \quad \eta_T^* = \exp[\theta(1 - T^*)], \quad (1)$$

90 where viscosity is normalized by reference viscosity η_0 defined at $T^* = 1$. Temperature is
 91 normalized as

$$92 \quad T^* = \frac{T - T_s}{\Delta T}, \quad (2)$$

93 where T_s is the surface temperature (~ 273 K), and ΔT is the (arbitrary) temperature scale. The
 94 degree of temperature dependency is controlled by the Frank-Kamenetskii parameter θ , which

95 can be related to the activation energy E as [e.g., *Solomatov and Moresi, 2000*]

$$96 \quad \theta = \frac{E\Delta T}{R(T_s + \Delta T)^2}, \quad (3)$$

97 where R is the universal gas constant. For E of $\sim 300 \text{ kJ mol}^{-1}$ [e.g., *Karato and Wu, 1993*]
 98 and ΔT of $\sim 1300 \text{ K}$, for example, θ is ~ 20 .

99 The coldest part of the lithosphere would be very stiff due to this strongly temperature-
 100 dependent viscosity, but it can also deform by brittle failure. In the continuum limit, this brittle
 101 behavior can be modeled by nonlinear effective viscosity that is adjusted to ensure the stresses
 102 remain bounded by the yield stress envelope [*Moresi and Solomatov, 1998*]. The yield stress
 103 criterion for brittle deformation may be expressed as

$$104 \quad \tau_y = c_0 + \mu \rho_0 g z, \quad (4)$$

105 where c_0 is the cohesive strength, μ is the friction coefficient, ρ_0 is reference density, g is
 106 gravitational acceleration, and z is depth. Using the length scale D , which is the depth of a
 107 fluid layer, and the stress scale $\eta_0 \kappa / D^2$, where κ is thermal diffusivity, the criterion may be
 108 nondimensionalized as

$$109 \quad \tau_y^* = \tau_0^* + \tau_1^* z^*, \quad (5)$$

110 where

$$111 \quad \tau_0^* = \frac{c_0 D^2}{\kappa \eta_0}, \quad (6)$$

112 and

$$113 \quad \tau_1^* = \frac{\mu \rho_0 g D^3}{\kappa \eta_0}. \quad (7)$$

114 Using the Rayleigh number defined as

$$115 \quad Ra = \frac{\alpha \rho_0 g \Delta T D^3}{\kappa \eta_0}, \quad (8)$$

116 where α is thermal expansivity, the criterion can also be expressed as

$$117 \quad \tau_y^* = \tau_0^* + \gamma Ra z^*, \quad (9)$$

118 where

$$119 \quad \gamma = \frac{\mu}{\alpha \Delta T}. \quad (10)$$

120 In this study, the cohesive strength is assumed to be negligibly small compared to the
 121 depth-dependent component, and τ_0^* is set to $\tau_1^* \times 10^{-5}$. This is a reasonable approximation
 122 given experimental data on rock friction at low hydrostatic pressure [e.g., *Byerlee, 1978*]
 123 and also allows me to focus on the single parameter γ . Note that a nonzero cohesive
 124 strength term appearing for experimental data at high confining pressures could arise from a
 125 pressure-dependent friction coefficient with zero cohesive strength.

126 The nonlinear effective viscosity for the plastic deformation is calculated as

$$127 \quad \eta_y^* = \frac{\tau_y^*}{e_{II}^*}, \quad (11)$$

128 where e_{II}^* is the second invariant of the (nondimensionalized) strain rate tensor. The transition
 129 between plastic and ductile deformation is handled by using the harmonic mean of the
 130 temperature-dependent viscosity and the above effective viscosity as

$$131 \quad \eta^* = \left(\frac{1}{\eta_T^*} + \frac{1}{\eta_y^*} \right)^{-1}. \quad (12)$$

132 The effective viscosity for plastic deformation η_y^* is calculated for any deformation, but when
 133 stresses are smaller than the yield stress (i.e., η_y^* is large), the harmonic mean above will be
 134 dominated by η_T^* .

135 The linear-exponential form of temperature-dependent viscosity [equation (1)] predicts
 136 much smaller viscosity variation across the entire lithosphere than the more realistic Arrhenius
 137 form, $\exp(E/RT)$, but because the above pseudoplastic rheology effectively eliminates
 138 a drastic viscosity increase in the upper half of the lithosphere, the difference between

139 the linear-exponential and Arrhenius forms is actually small [Solomatov, 2004]. It is still
 140 important to use the realistic value of θ as it controls the strength of the lower half of the
 141 lithosphere.

142 When considering the effects of mantle melting, I will add depth-dependent viscosity as

$$143 \quad \eta^* = \left(\frac{1}{\eta_T^* Z(z^*)} + \frac{1}{\eta_y^*} \right)^{-1}, \quad (13)$$

144 where

$$145 \quad Z(z^*) = \begin{cases} \Delta\eta & \text{for } z^* \leq h^* \\ 1 & \text{for } z^* > h^* \end{cases} \quad (14)$$

146 where h^* is the thickness of dehydrated mantle and $\Delta\eta$ is a viscosity contrast introduced by
 147 dehydration.

148 **2.2. Governing Equations and Heating Mode**

149 The nondimensionalized governing equations for thermal convection of an incompressible
 150 fluid consist of the conservation of mass,

$$151 \quad \nabla \cdot \mathbf{u}^* = 0, \quad (15)$$

152 the conservation of momentum,

$$153 \quad -\nabla P^* + \nabla \cdot [\eta^* (\nabla \mathbf{u}^* + \nabla \mathbf{u}^{*T})] - Ra T^* \mathbf{e}_z = 0, \quad (16)$$

154 and the conservation of energy,

$$155 \quad \frac{\partial T^*}{\partial t^*} + \mathbf{u}^* \cdot \nabla T^* = \nabla^2 T^* + H^*. \quad (17)$$

156 The unit vector pointing downward is denoted by \mathbf{e}_z . The spatial coordinates are normalized
 157 by the length scale D , and time is normalized by the diffusion time scale, D^2/κ . Velocity \mathbf{u}^*
 158 is thus normalized by κ/D . Dynamic pressure P^* and heat generation H^* are normalized by

159 $\eta_0 \kappa / D^2$ and $k \Delta T / (\rho_0 D^2)$, respectively, where k is thermal conductivity.

160 In this study, I will focus on thermal convection that is purely internally heated, by
 161 using the insulated bottom boundary condition. There will be no thermal boundary layer at
 162 the bottom, simplifying the scaling analysis of numerical results. This heating mode is also
 163 appropriate for the majority of the Earth history [Korenaga, 2008a, section 5.1]. At the same
 164 time, a temperature contrast across the fluid layer is not known *a priori*, so the maximum
 165 temperature, T_{\max}^* , is not guaranteed to be unity. Some *a posteriori* rescaling is thus necessary.
 166 The Frank-Kamenetskii parameter is recalculated from its original value θ_0 as

$$167 \quad \theta = \theta_0 T_{\max}^*, \quad (18)$$

168 so that $\exp(\theta)$ corresponds to the actual maximum viscosity variation due to temperature
 169 dependency. The internal Rayleigh number may also be defined with T_{\max}^* as

$$170 \quad Ra_i = Ra T_{\max}^* \exp[\theta_0 (T_{\max}^* - 1)], \quad (19)$$

171 in which the total temperature contrast is $T_{\max}^* \Delta T$, and the internal viscosity, η_i , is assumed
 172 to be $\eta_0 \exp[\theta_0 (1 - T_{\max}^*)]$. Because of purely internal heating, the surface heat flux q is, at a
 173 statistical equilibrium, equal to total heat generation in the fluid divided by surface area

$$174 \quad q = \rho_0 D H, \quad (20)$$

175 and the corresponding Nusselt number is calculated as

$$176 \quad Nu = \frac{q}{k T_{\max}^* \Delta T / D} = \frac{H^*}{T_{\max}^*}. \quad (21)$$

177 The internal heating ratio (IHR), ξ , is the difference between heat flux out of the top
 178 boundary and that into the bottom boundary, normalized by the former [e.g., McKenzie *et al.*,
 179 1974], i.e.,

$$180 \quad \xi = \frac{Nu_{\text{top}} - Nu_{\text{bot}}}{Nu_{\text{top}}}, \quad (22)$$

181 and because the bottom boundary is insulated in this study ($Nu_{\text{bot}}=0$), IHR is unity for all runs
 182 as long as H^* is positive. The internal heat production H^* does not directly correspond to
 183 the amount of radiogenic heat production in the mantle, which may be referred here as H_{rad}^* .
 184 Over the Earth history, the mantle has been (usually) cooling with time [Abbott *et al.*, 1994;
 185 Herzberg *et al.*, 2010], and in the study of mantle convection, this secular cooling is often
 186 included as part of ‘internal’ heating. So H^* represents both radiogenic heat production and
 187 secular cooling. Secular cooling is a transient phenomenon, and directly simulating it requires
 188 us to assume an initial condition for subsolidus mantle convection on Earth, which is hardly
 189 known. Numerical models for mantle convection are therefore typically run for a number of
 190 convective overturns to reach a statistical equilibrium so that model results do not strongly
 191 depend on employed initial conditions. This steady-state modeling approach has to include
 192 secular cooling as part of internal heating, in order to simulate an Earth-like IHR. The thermal
 193 evolution of Earth can be studied reasonably well by assuming that the mantle is in a quasi
 194 steady state at each time step [e.g., Daly, 1980].

195 It is important to distinguish IHR from the convective Urey ratio, Ur , which is the ratio
 196 of radiogenic heat production in the mantle over the mantle heat flux [Christensen, 1985], i.e.,

$$197 \quad Ur = \frac{H_{\text{rad}}^*}{Nu_{\text{top}}}. \quad (23)$$

198 The Urey ratio is directly related to the chemical composition of Earth’s mantle, and it is a
 199 key parameter to describe the thermal budget of Earth. When Ur is discussed, radiogenic heat
 200 production and secular cooling are considered separately. As noted by Korenaga [2008a],
 201 there has been some misunderstanding in the literature by confusing Ur with IHR or by
 202 underestimating the significance of secular cooling, and unfortunately, such confusion still
 203 seems to continue [e.g., Deschamps *et al.*, 2010]. IHR can be related to the convective Urey
 204 ratio as [Korenaga, 2008a]

$$205 \quad \xi \approx 1 - \frac{C_c}{C_m + C_c}(1 - Ur), \quad (24)$$

206 where C_m and C_c are, respectively, the heat capacities of the mantle and the core. The

207 present-day Urey ratio is probably ~ 0.2 [Korenaga, 2008a], but because the core heat capacity
 208 is only $\sim 1/5$ of the whole Earth value, the present-day IHR for Earth's mantle is estimated
 209 to be ~ 0.9 [Korenaga, 2008a]. Based on thermal history considerations, the Urey ratio may
 210 have been higher in the past [Korenaga, 2006; Herzberg *et al.*, 2010], so IHR is likely to have
 211 been closer to unity than at present. To first order, therefore, the use of purely internal heating
 212 ($\xi=1$) appears to be a reasonable simplification.

213 **2.3. Notes on Modeling Strategy**

214 Besides the use of pseudoplastic rheology, the numerical model of mantle convection as
 215 specified in the previous sections is kept simple to facilitate the interpretation of modeling
 216 results, and the potential significance of realistic complications, which are neglected in this
 217 study, are discussed in the following.

218 Because of the insulating boundary condition, bottom heat flux is zero, so there are no
 219 upwelling plumes in the model. The influence of plumes on plate dynamics thus cannot be
 220 examined. Because of the nearly unity IHR expected for Earth's mantle (§2.2), however,
 221 such influence may not be of first order. The governing equations employed are based on
 222 the Boussinesq approximation [e.g., Schubert *et al.*, 2001], so adiabatic gradients are zero
 223 (i.e., the total temperature contrast $T_{\max}^* \Delta T$ is the superadiabatic temperature contrast), and
 224 the model temperature corresponds to potential temperature. The effects of compressibility
 225 on the gross characteristics of thermal convection have been known to be rather minor
 226 [Jarvis and McKenzie, 1980; Bercovici *et al.*, 1992].

227 For the ductile deformation of the mantle, the Newtonian rheology with linear-exponential
 228 temperature dependency is adopted [equation (1)], but mantle rheology is known to be much
 229 more complex depending on, at least, stress, pressure, grain size, and chemical composition
 230 [e.g., Karato and Wu, 1993]. In case of pseudoplastic rheology, the difference between the
 231 Arrhenius rheology and its linear-exponential approximation is not important as already
 232 mentioned, and I choose to use the latter because it is specified by only one nondimensional
 233 parameter θ , whereas the Arrhenius-type temperature dependency requires three [e.g.,
 234 Korenaga, 2009]. Non-Newtonian, stress-dependent rheology can be approximated by

235 Newtonian rheology if the activation energy is properly scaled [*Christensen, 1984*]. The
236 importance of pressure dependence caused by the activation volume is not clear at the
237 moment. First of all, activation volumes for mantle rheology are still poorly known even
238 for upper mantle minerals [*Korenaga and Karato, 2008*]. Second, viscosity increase with
239 increasing pressure should be at least partly cancelled by viscosity decrease with increasing
240 temperature along the mantle adiabat. With the Boussinesq approximation employed here,
241 the use of pressure-independent rheology actually requires non-zero activation volume, the
242 effect of which is assumed to be cancelled exactly by temperature variations along the adiabat.
243 Grain size variation can affect mantle dynamics considerably [e.g., *Solomatov, 1996*], but
244 how grain size should evolve in the convecting mantle is still poorly understood, so it appears
245 premature to consider its effect in this study. The effect of composition on mantle rheology
246 is taken into account when dehydration stiffening is effected by depth-dependent viscosity
247 [equation (14)]. There are of course other compositional effects [e.g., *Karato, 2008*], but the
248 effect of dehydration appears to be most important at least for the upper mantle rheology
249 [e.g., *Karato et al., 1986; Mei and Kohlstedt, 2000a, b; Faul and Jackson, 2007*], and mantle
250 dehydration is always expected whenever mantle melts [*Hirth and Kohlstedt, 1996*].

251 Another important rheological aspect for large-scale mantle dynamics is a viscosity jump
252 at the base of the upper mantle, which has been estimated to be on the order of ~ 10 - 100
253 primarily through the geodynamical modeling of Earth's geoid [e.g., *Hager, 1984*]. Such
254 inference is, however, also known to suffer from considerable nonuniqueness [e.g., *King, 1995;*
255 *Kido and Cadek, 1997*], and the viscosities of the upper and lower mantle may not be very
256 different if the mantle transition zone has a lower viscosity [*Soldati et al., 2009*]. Furthermore,
257 even if the lower mantle does have a higher viscosity than the upper mantle, it applies only
258 for the present-day situation. When the mantle was hotter in the past, the viscosity contrast
259 may be smaller or even reversed if the lower mantle rheology is more temperature-dependent
260 (i.e., higher activation energy) than the upper mantle counterpart. Rheological stratification in
261 the mantle is an important subject, but these uncertainties imply a variety of situations to be
262 considered, so it is left for future studies.

263 The mantle transition zone is also characterized by multiple phase transitions, and

264 in particular, the effects of the endothermic phase change at the base of the transition
 265 zone on large-scale mantle circulation was once a popular topic in geodynamics [e.g.,
 266 *Christensen and Yuen, 1984; Tackley et al., 1993; Solheim and Peltier, 1994; Yuen et al.,*
 267 *1994*]. Numerical studies with strong plates exhibit, however, only a modest influence of
 268 endothermic phase change on mantle dynamics [e.g., *Zhong and Gurnis, 1994*], and recent
 269 experimental studies further suggest that the Clapeyron slope of the endothermic phase change
 270 is likely to be only -1.3 MPa K^{-1} [*Katsura et al., 2003; Fei et al., 2004*], which is much less
 271 negative than previously thought. Modeling phase transitions, therefore, is not considered to
 272 be essential.

273 Finally, the model is 2-D Cartesian, whereas the use of a 3-D spherical shell would be
 274 most appropriate. The restriction to 2-D modeling is primarily to generate a large number
 275 of modeling results (with modest computational resources) so that scaling analysis becomes
 276 more robust, though I do not expect scaling laws to change drastically by moving from 2-D to
 277 3-D. The effect of sphericity would likely be of minor nature [*Bercovici et al., 2000*]. Based
 278 on isoviscous convection models using 3-D spherical shells, for example, *Deschamps et al.*
 279 [*2010*] recently derived the following heat-flow scaling (adapted here for the case of purely
 280 internal heating),

$$281 \quad Nu \approx 0.59 f^{0.05} Ra^{0.300-0.003f}, \quad (25)$$

282 where f is the ratio of the core radius to the total radius of a planet. The ratio f is 0.55 for
 283 Earth and unity for Cartesian, so it can be seen that sphericity has virtually no impact on this
 284 scaling.

285 The convection model of this study is, therefore, simple but probably not simpler than
 286 necessary. In any event, this study should provide a reference point, by which the effects of
 287 any additional complication can be quantified in future.

288 **3. Numerical Results and Scaling Analysis**

289 The finite element code of *Korenaga and Jordan [2003]* was used to solve the coupled
 290 Stokes flow and thermal advection-diffusion equations (15)-(17). The benchmark tests of this

code can be found in *Korenaga and Jordan* [2003] for Newtonian rheology and in *Korenaga* [2009] for non-Newtonian rheology. To reduce wall effects, the aspect ratio of the convection model is set to 8, and the model domain is discretized with 400×50 uniform 2-D quadrilateral elements. With this mesh resolution, model parameters are chosen so that Nu does not exceed 20 and the top thermal boundary layer contains at least a few elements vertically on average. The nondimensional surface temperature is fixed to zero, and the bottom boundary is insulated. The top and bottom boundaries are free-slip, and a reflecting boundary condition is applied to the side boundaries. In all cases, Ra is set to 10^6 , but Ra_i varies greatly because of different combinations of θ_0 and H^* (and thus T_{\max}^*).

The initial temperature condition is specified as

$$T^*(x^*, z^*) = z^* + a \cos(\pi x^*) \sin(\pi z^*) + \varepsilon, \quad (26)$$

where a is usually 0.2, and ε is random fluctuation with the amplitude of 10^{-3} . When the assumed mantle rheology is appropriate for the operation of plate-tectonic convection, this initial condition quickly brings the system to that mode of convection. Otherwise, the system gradually migrates into the mode of stagnant-lid convection. If I start with a uniformly hot fluid instead, the system always begins with stagnant-lid convection, and sublithospheric mantle is heated up considerably until the onset of plate tectonics. Very low viscosity (and thus very high convective velocity) beneath the stagnant lid during this initial period means exceedingly small time steps for numerical integration, so this type of initial condition is not computationally efficient when aiming at statistically steady states required for scaling analysis.

3.1. Convection Diagnostics

A typical snapshot of model run is shown in Figure 1a. This is the case of $\gamma=0.6$, $\theta_0=15$, and $H^*=20$, with the standard pseudoplastic rheology [equation (12)]. In addition to T_{\max}^* , I calculate two more measures for the temperature scale. One is the domain-average

316 temperature,

$$317 \quad \langle T^* \rangle = \iint T^* dx^* dz^* / \iint dx^* dz^* , \quad (27)$$

318 and the other is the (self-consistent) internal temperature [Korenaga, 2009],

$$319 \quad T_i^* = \frac{1}{1 - \delta'} \int_{\delta'}^1 \left(\int T^* dx^* / \int dx^* \right) dz^* , \quad (28)$$

320 where $\delta' = T_i^*/H^*$.

321 The vigor of convection can be quantified by calculating the root-mean-square
322 velocity v_{rms}^* , and a velocity diagnostic most indicative of the mode of convection is the
323 root-mean-square surface velocity v_s^* . To quantify how plate-like the surface velocity field is,
324 *Weinstein and Olson* [1992] introduced the notion of ‘plateness’, and for convection exhibiting
325 multiple plates with different velocities, I use the following definition of plateness,

$$326 \quad P_x = \int_{e' < x} dx^* / \int dx^* , \quad (29)$$

327 where

$$328 \quad e' = \frac{1}{v_s^*} \left| \frac{dv^*(z^* = 0)}{dx^*} \right|. \quad (30)$$

329 The parameter P_x measures the fraction of surface with normalized strain rate e' smaller than
330 the given threshold x . The velocity profile shown in Figure 1b, for example, has $P_{0.1}$ of 0.76
331 (Figure 1c). Like other definitions of plateness, P_x varies from 0 to 1, with higher values
332 corresponding to more rigid behavior. For comparison, actual plates on Earth tend to have
333 wide diffuse boundary zones, which occupy $\sim 15\%$ of the surface area at the present day
334 [*Gordon and Stein*, 1992].

335 To understand the spatial distribution of viscous dissipation, I define Φ_c as the viscous
336 dissipation within the region above $z^* = c$,

$$337 \quad \Phi_c = \int_0^c \left(\int \eta^* e_{ij}^* e_{ij}^* dx^* \right) dz^* , \quad (31)$$

338 and calculate Φ_δ , $\Phi_{\delta/2}$, and Φ ($\equiv \Phi_1$), where δ is (on average) the maximum thickness of the

339 top thermal boundary layer [e.g., *Busse*, 1967],

$$340 \quad \delta = 2Nu^{-1}. \quad (32)$$

341 Here δ is nondimensionalized by the model depth D .

342 Each case was run up to $t^* = 6$. The cumulative heat generation and cumulative heat loss
 343 from the surface are monitored, and when these two start to match within $\sim 1\%$, I judge that
 344 the system has reached statistically steady state. This usually takes place at $t^* \approx 2 - 3$, and I
 345 use subsequent model results to calculate time-average values of key diagnostics such as Nu
 346 and Φ . The (one) standard deviation of time-averaged Nu is typically less than 1%, whereas
 347 the standard deviation of Nu itself is often greater by one order of magnitude, reflecting the
 348 highly time-dependent nature of convection (Figure 1d). Surface velocity exhibits even greater
 349 time dependency (Figure 1e).

350 **3.2. Reference Scaling**

351 A total of 82 cases were run with the standard pseudoplastic rheology using different
 352 combinations of γ (0.1-1), θ_0 (10-25), and H^* (8-20). The summary of convection diagnostics
 353 is reported in Tables A1 and A2; eight runs resulted in stagnant-lid convection, and others
 354 exhibited plate-tectonic convection.

355 Three different temperature scales, T_{\max}^* , $\langle T^* \rangle$, and T_i^* , are correlated well to each other
 356 (Figure 2a). Regardless of the mode of convection, T_{\max}^* is distinctly higher than $\langle T^* \rangle$, and this
 357 is because the thickness of the top thermal boundary layer is not trivial in those runs. The
 358 maximum Nu achieved is only ~ 20 (Figure 2b), and these different temperature scales are
 359 expected to converge as Nu increases. Stagnant-lid runs are characterized by similar T_{\max}^* and
 360 T_i^* , because of small temperature variations beneath the stagnant lid.

361 The relation between Nu and Ra_i appears to roughly follow the classical scaling of
 362 $Nu \propto Ra_i^{1/3}$ within runs with the same γ and similar θ (Figure 2b). Varying γ has considerable
 363 effects on the scaling of Nu as well as v_{rms}^* (Figure 2c). The distinction between plate-tectonic
 364 and stagnant-lid runs is very clear in the correlation (or lack thereof) between v_{rms}^* and v_s^*

365 (Figure 2). Average surface velocity in these plate-tectonic runs is higher than corresponding
 366 v_{rms}^* because the latter involves averaging over the entire domain, the majority of which moves
 367 more slowly than surface plates.

368 My scaling analysis to understand the systematics of these model results is based on
 369 the local stability of top thermal boundary layer [Howard, 1966]. Because of pseudoplastic
 370 rheology, the effective viscosity of the top boundary layer or the effective lithospheric
 371 viscosity, η_L , is expected to be higher than the interior viscosity, and I denote the viscosity
 372 contrast between them as

$$373 \quad \Delta\eta_L = \eta_L/\eta_i. \quad (33)$$

374 Viscosity in the top thermal boundary layer varies considerably as specified by equation (12),
 375 and the effective lithospheric viscosity is an attempt to capture the overall stiffness of the
 376 boundary layer by just one viscosity value. For the stiff boundary layer to subduct, it has to
 377 become convectively unstable at least, and by assuming that the maximum thickness of the
 378 boundary layer δD corresponds to marginal stability, the following relation should hold:

$$379 \quad \frac{\alpha\rho_0g(T_{\text{max}}^*\Delta T)(\delta D)^3}{\kappa\eta_L} = Ra_c, \quad (34)$$

380 where Ra_c is the critical Rayleigh number. By using the relation between δ and Nu
 381 [equation (32)], this marginal stability criterion may be rearranged as

$$382 \quad Nu = 2 \left(\frac{Ra_i}{Ra_c} \right)^{1/3} \Delta\eta_L^{-1/3}, \quad (35)$$

383 or

$$384 \quad \Delta\eta_L = \frac{8Ra_i}{Ra_c Nu^3}. \quad (36)$$

385 Hereinafter Ra_c is set to 10^3 .

386 Equation (36) may be regarded as a way to extract lithospheric viscosity contrasts
 387 from the measured pairs of Ra_i and Nu . The lithospheric viscosity contrast calculated this
 388 way increases as θ increases, and this θ sensitivity is greater for higher γ (Figure 3a). The

389 following functionality appears to be sufficient to reproduce the first-order behavior of the
 390 viscosity contrast,

$$391 \quad \Delta\eta_L(\gamma, \theta) = \exp[a(\gamma)\theta], \quad (37)$$

392 which converges to unity at the limit of zero θ . The coefficient $a(\gamma)$ is determined by linear
 393 regression for each group of runs with the same γ (Figure 3a). Excluding the result for γ of
 394 0.1, the runs with which are characterized by rather low plateness (Table A1), the coefficient
 395 is linearly correlated with γ in the logarithmic space (Figure 3b), which may be expressed as

$$396 \quad a(\gamma) \approx 0.327\gamma^{0.647}. \quad (38)$$

397 Equations (37) and (38) can predict $\Delta\eta_L$ reasonably well over the range of four orders of
 398 magnitude (Figure 3c). The prediction for Nu through equation (35) has the average error
 399 of $\sim 10\%$ (Figure 3d). This error is considerably larger than that observed for the heat-flow
 400 scaling derived by *Moresi and Solomatov* [1998], which was based on convection with the
 401 aspect ratio of one. The use of the wide aspect ratio ($= 8$) in this study and resultant time
 402 dependency in convection patterns may be the source of these scatters.

403 The lithospheric viscosity contrast $\Delta\eta_L$ calculated from equation (36) exhibits broad
 404 correlations with other convection diagnostics (Figure 4). Higher $\Delta\eta_L$ generally gives rise
 405 to higher plateness (Figure 4a) and greater viscous dissipation in the top boundary layer
 406 (Figure 4c). How viscous dissipation is distributed within the boundary layer, however, seems
 407 to be insensitive to variations in $\Delta\eta_L$ as $\Phi_{\delta/2}/\Phi_{\delta} \sim 0.5-0.6$ for all of plate-tectonic runs
 408 (Figure 4d).

409 Assuming the half-space cooling of lithosphere, the (average) maximum plate thickness
 410 δ is related to the average length of plates, L , as

$$411 \quad \delta \sim 2 \left(\frac{L}{Dv_s^*} \right)^{1/2}, \quad (39)$$

412 where $L/(Dv_s^*)$ is the average time from a ridge to a subduction zone. Thus, the average aspect

413 ratio of convection cells may be calculated from Nu and v_s^* as

$$414 \quad \frac{L}{D} = \frac{v_s^*}{Nu^2}, \quad (40)$$

415 for which equation (32) is used. The aspect ratio gradually increases as $\Delta\eta_L$ increases, i.e.,
 416 stronger plates tend to be longer (Figure 4b). By assuming some empirical relation for L/D
 417 (e.g., $L/D \sim \Delta\eta_L^{1/6}$), equation (40) may be rearranged as scaling for v_s^* ,

$$418 \quad v_s^* = 4 \left(\frac{L}{D} \right) \left(\frac{Ra_i}{Ra_c} \right)^{2/3} \Delta\eta_L^{-2/3}. \quad (41)$$

419 That is, unlike the scaling for heat flux [equation (35)], some information on the aspect ratio
 420 of convection cells is essential for the scaling for surface velocity.

421 **3.3. Effect of Shallow Stiffening**

422 On Earth, the creation of new plates at mid-ocean ridges is usually accompanied by the
 423 melting of upwelling mantle (unless the mantle is too cold), and this chemical differentiation
 424 along the global mid-ocean ridge system constitutes the dominant fraction of terrestrial
 425 magmatism [Crisp, 1984]. This mantle melting results in the formation of oceanic crust as
 426 well as depleted mantle lithosphere, both of which are chemically more buoyant with respect
 427 to the underlying asthenosphere [Oxburgh and Parmentier, 1977], and the depleted lithosphere
 428 also becomes intrinsically more viscous (by $\sim 10^3$) because of dehydration caused by melting
 429 [Hirth and Kohlstedt, 1996]. As long as plate tectonics is taking place, the chemical buoyancy
 430 of oceanic lithosphere is insignificant as resistance to subduction because the basalt-to-eclogite
 431 transition at relatively shallow depth (< 60 km) makes the subducting slab compositionally
 432 denser than the surrounding mantle [e.g., Ringwood and Irifune, 1988]. In this study, therefore,
 433 I focus on the effect of dehydration stiffening on the scaling of plate-tectonic convection. As
 434 in Korenaga [2009], instead of tracing the advection of the dehydrated slab through time, I
 435 use the depth-dependent viscosity that is fixed in time [equation (14)]. Though the subducting
 436 slab loses the extra viscosity contrast $\Delta\eta$ as soon as it passes the given depth h^* , the effect of

437 shallow stiffening on slab bending can still be evaluated with this scheme.

438 The scaling of Nu [equation (35)] indicates that different combinations of Ra_i and $\Delta\eta_L$
 439 can produce the same Nu . Thus, in terms of the efficiency of heat transport, a run with high
 440 Ra_i and high $\Delta\eta_L$ may be indistinguishable from that with low Ra_i and low $\Delta\eta_L$, but shallow
 441 stiffening may affect these cases differently. A wide variety of plate-tectonic cases were
 442 thus simulated by varying γ (0.4-0.8), θ_0 (10-25), and H^* (2-20), and shallow stiffening was
 443 incorporated with h^* ranging from 0.1 to 0.3 and $\Delta\eta$ ranging from 3 to 10^3 . Stiffening by
 444 mantle melting is limited mostly to the top 200 km or so (i.e., $h^* < 0.07$), and the use of
 445 greater h^* is to study the asymptotic behavior of stiffening effects. Also, the top thermal
 446 boundary layer in numerical modeling is thicker than actual oceanic lithosphere because of
 447 relatively low Ra_i used in this study, so h^* has to be comparably large in order to reproduce an
 448 Earth-like combination of thermal and compositional boundary layers. The number of runs is
 449 225 in total, with 19 stagnant-lid runs (Tables A3-A8). Convection diagnostics were measured
 450 in the same way for reference runs.

451 The scaling analysis for runs with shallow stiffening is founded on that for the reference
 452 runs. As in the previous section, the lithospheric viscosity contrast $\Delta\eta_L$ is calculated from the
 453 measured pair of Nu and Ra_i . A key issue is how this viscosity contrast is influenced by the
 454 additional depth-dependent viscosity, and this influence may be measured by the deviation
 455 from the prediction based on equation (37). The predicted viscosity contrast is based solely on
 456 γ and θ , and it is denoted as $\Delta\eta_{L,\text{ref}}$ to distinguish from the actual $\Delta\eta_L$. The ratio $\Delta\eta_L/\Delta\eta_{L,\text{ref}}$
 457 is loosely correlated with $\Delta\eta$ and h^* as one may expect (Figure 5a,b); higher $\Delta\eta$ or h^* leads to
 458 higher $\Delta\eta_L$ than predicted by equation (37). A better correlation may be seen between the two
 459 ratios, $\Delta\eta_L/\Delta\eta_{L,\text{ref}}$ and h^*/h_{ref}^* (Figure 5c), where h_{ref}^* is defined as

$$460 \quad h_{\text{ref}}^* = Nu_{\text{ref}}^{-1}, \quad (42)$$

461 and

$$462 \quad Nu_{\text{ref}} = 2 \left(\frac{Ra_i}{Ra_c} \right)^{1/3} \Delta\eta_{L,\text{ref}}^{-1/3}. \quad (43)$$

463 The parameter h_{ref}^* is the averaged thickness of the top thermal boundary layer expected for
 464 a run with the same Ra_i but with the standard pseudoplastic rheology. The ratio $\Delta\eta_L/\Delta\eta_{L,\text{ref}}$
 465 increases as h^*/h_{ref}^* but eventually saturates and never exceeds the given $\Delta\eta$. This behavior
 466 may be represented by the following functionality,

$$467 \quad \Delta\eta_L = \Delta\eta_{L,\text{ref}} \exp \left[\ln(\Delta\eta) \max \left(1, \frac{h^*}{\chi h_{\text{ref}}^*} \right) \right], \quad (44)$$

468 which means that $\Delta\eta_L$ converges to the simple product of $\Delta\eta_{L,\text{ref}}$ and $\Delta\eta$ when h^* is
 469 sufficiently greater than h_{ref}^* . The parameter χ controls how high h^* should be with respect
 470 to h_{ref}^* in order to achieve the convergence; greater χ means that thicker h^* is required. By
 471 trying a range of values, I found that $\chi \approx 6$ can reproduce the measured $\Delta\eta_L$ reasonably well
 472 (Figure 5d).

473 The relations between $\Delta\eta_L$ and other convection diagnostics are more ambiguous than
 474 observed for the reference runs (Figure 6). It appears to be premature to parameterize the
 475 aspect ratio L/D as a simple function of the lithospheric viscosity contrast (Figure 6b), and
 476 more thorough work is clearly required to better understand the self-organization of plate
 477 tectonics. It is still interesting to note, however, that high plateness is possible even with low
 478 viscosity contrast (Figure 6a) and that plate-tectonic convection can occur even when most of
 479 viscous dissipation takes place in the top boundary layer (Figure 6c).

480 **3.4. Conditions for Plate-Tectonic Convection**

481 The condition for plate-tectonic convection is found to be seen most clearly in the
 482 covariation of Ra_i and $\Delta\eta_L$ (Figure 7). Plate-tectonic convection is possible even with high
 483 lithospheric viscosity contrast if Ra_i is sufficiently high, and the critical viscosity contrast,
 484 above which plate-tectonic convection is unlikely, appears to be

$$485 \quad \Delta\eta_{L,\text{crit}} \approx 0.25 Ra_i^{1/2}, \quad (45)$$

486 though there are a few runs that slightly violate this threshold.

487 To understand the meaning of this scaling, I consider stress balance at the bending of
 488 subducting slab, which is probably the most critical part of plate-tectonic convection. First,
 489 the stress due to the negative buoyancy of the slab may be expressed as

$$490 \quad \tau_S \sim \alpha \rho_0 g (T_{\max}^* \Delta T) D, \quad (46)$$

491 or by normalizing the (internal) stress scale, $\eta_i \kappa / D^2$,

$$492 \quad \tau_S^* \sim Ra_i. \quad (47)$$

493 Second, the bending stress should be proportional to the lithospheric viscosity and bending
 494 strain rate as [e.g., *Conrad and Hager, 1999*]

$$495 \quad \tau_B \sim \eta_L \frac{v_s(\delta D)}{R^2}, \quad (48)$$

496 where R is the radius of curvature, and its nondimensionalized form is

$$497 \quad \tau_B^* \sim \Delta \eta_L v_s^* \delta \left(\frac{D}{R} \right)^2 \propto \Delta \eta_L^{2/3} Ra_i^{1/3} \left(\frac{D}{R} \right)^2. \quad (49)$$

498 Finally, by assuming $\tau_S \approx \tau_B$ at $\Delta \eta_L = \Delta \eta_{L,\text{crit}}$, we may derive the following scaling for the
 499 radius of curvature,

$$500 \quad \frac{R}{D} \propto Ra_i^{-1/6}. \quad (50)$$

501 Thus, the radius is weakly dependent of the vigor of convection, and it becomes smaller
 502 for more vigorous convection. Without this variation in the radius of curvature, the critical
 503 viscosity contrast would be more sensitive to a change in Ra_i (i.e., proportional to Ra_i instead
 504 of $Ra_i^{1/2}$).

505 Note that all of 307 runs reported here are either strictly plate-tectonic or stagnant-lid
 506 convection, and there is no case of episodic overturn, in which the system periodically
 507 goes back and forth between plate-tectonic and stagnant-lid modes [*Moresi and Solomatov,*

1998]. This is consistent with the use of virtually zero cohesion strength and finite friction coefficient in this study (§2.1), because the possibility of the episodic overturn mode appears to be important only with nontrivial cohesion strength [e.g., *Moresi and Solomatov*, 1998; *Stein et al.*, 2004; *O’Neill et al.*, 2007]. The use of purely internal heating (thus the lack of upwelling plumes) in this study might also be responsible.

4. Discussion and Conclusion

On the basis of the scaling of Nu [equation (35)] and the parameterization of $\Delta\eta_L$ [equations (37), (38), and (44)], it is now possible to discuss the relation between mantle temperature and surface heat flux, which is fundamental to our theoretical understanding of the long-term evolution of Earth. Because some of key model parameters are still poorly known [e.g., *Korenaga and Karato*, 2008], the following exercise should be regarded as a preliminary case study. As explained below, the self-consistent construction of a plausible heat-flow scaling law requires modeling the thermal and chemical evolution of Earth at the same time, so a more extensive exploration of the scaling of plate tectonics will be reported elsewhere.

First, for the dependency of viscosity on mantle potential temperature T_p , the following Arrhenius form is used,

$$\eta_T(T_p) = \eta_r \exp\left(\frac{E}{RT_p} - \frac{E}{RT_r}\right), \quad (51)$$

where η_r is reference viscosity at $T_p = T_r$, and E is assumed to be 300 kJ mol⁻¹ [*Korenaga*, 2006]. The reference temperature is set to 1623 K (1350°C), which corresponds to the present-day potential temperature of the ambient mantle [*Herzberg et al.*, 2007]. The Frank-Kamenetskii parameter θ is calculated from equation (3), and the reference lithospheric viscosity contrast $\Delta\eta_{L,\text{ref}}$ is calculated with γ of 0.8, which corresponds to the effective friction coefficient of ~ 0.02 [equation (10)].

The internal Rayleigh number Ra_i is then calculated with the above temperature-viscosity and the following values: $\alpha = 2 \times 10^{-5} \text{ K}^{-1}$, $\rho_0 = 4000 \text{ kg m}^{-3}$, $g = 9.8 \text{ m s}^{-2}$, and $D = 2900 \times 10^3 \text{ m}$. The dehydration of the mantle beneath mid-ocean ridges is assumed to

535 take place when the upwelling mantle crosses the solidus for dry pyrolitic mantle, and the
 536 initial pressure of melting (in GPa) can be calculated from the potential temperature (in K) as
 537 [*Korenaga et al.*, 2002]

$$538 \quad P_o = (T_p - 1423)/100, \quad (52)$$

539 and the thickness of dehydrated mantle h_m is given by $P_o/(\rho_o g)$. The nondimensional
 540 thickness h^* is h_m/D , and the viscosity contrast due to dehydration $\Delta\eta$ is assumed to be 10^2
 541 here. The lithospheric viscosity contrast $\Delta\eta_L$ gradually increases for higher T_p (Figure 8c,
 542 case 1) because hotter mantle starts to melt deeper (Figure 8b), but the effect of shallow
 543 stiffening on the viscosity contrast saturates at $T_p \sim 1600^\circ\text{C}$, above which the contrast slightly
 544 decreases because of smaller θ for higher T_p [equation (3)].

545 Lastly, the global heat flux Q is calculated as

$$546 \quad Q = kAT_p Nu/D, \quad (53)$$

547 where A is the surface area of Earth, and k is assumed to be $4 \text{ W m}^{-1} \text{ K}^{-1}$. The reference
 548 viscosity η_r is set to 10^{19} Pa s so that the predicted global heat flux matches the present-day
 549 convective heat flux of $\sim 38 \text{ TW}$ [*Korenaga*, 2008a] (Figure 8d, case 1). The effect of shallow
 550 stiffening suppresses the heat flux considerably and even reverts the sense of temperature
 551 sensitivity; the flux is lower for higher T_p above $\sim 1450^\circ\text{C}$ until the effect of shallow stiffening
 552 becomes saturated at $\sim 1600^\circ\text{C}$. For the temperature range of $1350\text{-}1600^\circ\text{C}$, which is most
 553 relevant to the thermal evolution of Earth for the last 3.5 Gyr [*Herzberg et al.*, 2010], the
 554 predicted relation between the mantle temperature and surface heat flux closely resembles that
 555 suggested by *Korenaga* [2006] along a similar line of reasoning but on the basis of the global
 556 energy balance.

557 Note that the reference viscosity η_r of 10^{19} Pa s (at present-day potential temperature)
 558 may be appropriate for asthenosphere but would typically be regarded as too low to represent
 559 the whole mantle, for which the viscosity of $10^{21}\text{-}10^{22} \text{ Pa s}$ is usually assumed. The effective
 560 lithospheric viscosity contrast is $\sim 3 \times 10^2$ in this example (Figure 8c), which is comparable to

561 the discrepancy. Traditionally, the average viscosity of the present-day mantle is estimated to
 562 be of that magnitude, in order to explain surface heat flux (or equivalently, plate velocities)
 563 [e.g., *Hager, 1991; Bercovici et al., 2000*], because the aforementioned geoid-based studies
 564 (§2.3) can constrain only relative variations in viscosity and are insensitive to the absolute
 565 values of viscosity. The heat-flow scaling of equation (35) suggests that a lithospheric
 566 viscosity contrast alone could regulate surface heat flux without invoking a viscosity increase
 567 in the lower mantle.

568 The use of constant viscosity contrast for dehydration stiffening $\Delta\eta$ for the entire
 569 temperature range (thus implicitly over the entire Earth history) is equivalent to assuming
 570 that the water content of the convecting mantle does not change with time. If the mantle is
 571 drier than present, for example, the viscosity contrast would be smaller, and if the mantle is
 572 completely dry, mantle melting should not cause any viscosity change. By combining the
 573 thermal budget of Earth with geological constraints on sea level change and with the growth
 574 of continental crust, *Korenaga [2008b]* suggested that the volume of Earth's oceans is unlikely
 575 to have been constant with time and that the mantle may have been gradually hydrated by
 576 subduction starting with a very dry state in the Archean. As the second example (denoted
 577 as case 2 in Figure 8), I consider effective heat-flow scaling expected for this scenario. For
 578 simplicity, the mantle is assumed to have been hydrated linearly from the completely dry state
 579 to the present state, as it cooled from 1550°C, to 1350°C for the last ~ 3 Gyr [*Herzberg et al.,*
 580 *2010*]. For T_p greater than 1550°C, therefore the internal viscosity is intrinsically higher by
 581 $\Delta\eta$, and this viscosity contrast gradually diminishes as T_p approaches 1350°C. This is reflected
 582 in how Ra_i varies with T_p (Figure 8a, case 2). At the same time, the viscosity contrast due to
 583 mantle melting is unity at $T_p \geq 1550^\circ\text{C}$ and gradually increases to the full value $\Delta\eta$ at T_p of
 584 1350°C. The total lithospheric viscosity contrast $\Delta\eta_L$ in this scenario is much reduced than the
 585 previous example (Figure 8c), but because of the overall reduction in Ra_i , the surface heat flux
 586 is suppressed further, and the inverse relationship between mantle temperature and heat flux
 587 dominates heat-flow scaling during the mantle hydration period (Figure 8d). Obviously, this
 588 type of calculation should be done more self-consistently by modeling the thermal evolution of
 589 Earth together with its global water cycle, and what is presented here is only a crude estimate.

590 In both cases, the lithospheric viscosity contrast is always smaller than its threshold
 591 (Figure 8c), so plate-tectonic convection seems to be dynamically plausible throughout
 592 the Earth history, as long as surface water exists to hydrate the lithosphere and reduce the
 593 effective friction coefficient [Korenaga, 2007]. In particular, the gradually hydrating mantle
 594 (case 2) helps to maintain relatively small $\Delta\eta_L$ even with deeper mantle melting at higher T_p ,
 595 facilitating the operation of plate tectonics in the early Earth.

596 Though previous attempts to estimate the heat-flow scaling of plate tectonics [Korenaga,
 597 2003, 2006] have already predicted the inverse relation between mantle temperature and
 598 surface heat flux as indicated by Figure 8, there are a few important differences. First, because
 599 the effect of shallow stiffening eventually saturates [equation (44)], the inverse relation is
 600 restricted to a certain temperature range. This subtle behavior is difficult to derive from the
 601 global energy balance approach adopted by the previous studies. Second, the global energy
 602 balance can be exploited to derive heat-flow scaling by *assuming* the mode of convection, so
 603 whether plate-tectonic convection is plausible or not cannot be addressed. Finally, the energy
 604 balance approach has a few poorly constrained parameters, such as the radius of curvature
 605 for plate bending, effective lithospheric viscosity, and the aspect ratio of convection, and it is
 606 possible to obtain wildly different results by varying them independently [e.g., Davies, 2009].
 607 Though similarly suffering from parameter uncertainty (e.g., γ and $\Delta\eta$) and from the very
 608 assumption of the pseudoplastic rheology as well, the present study provides a fully dynamic
 609 framework in which heat flow, velocity, lithospheric viscosity, aspect ratio, and the radius of
 610 curvature are all connected in a self-consistent manner.

611 **Appendix A: Numerical results**

612 Tabulated are selected convection diagnostics for statistically steady-state solutions as
 613 described in the main text. The Rayleigh number Ra is 10^6 for all cases. Reference runs refer
 614 to calculations with the standard pseudoplastic rheology, and runs with shallow stiffening
 615 refers to those with additional depth-dependent viscosity.

616 **Acknowledgments.** This work was sponsored by the U.S. National Science Foundation under

617 grant EAR-0449517 and Microsoft A. Richard Newton Breakthrough Research Award. The author
618 thanks the Associate Editor and two anonymous referees for careful reviews.

References

- 619 **References**
- 620 Abbott, D., L. Burgess, J. Longhi, and W. H. F. Smith, An empirical thermal history of the Earth's
621 upper mantle, *J. Geophys. Res.*, *99*, 13,835–13,850, 1994.
- 622 Bercovici, D., The generation of plate tectonics from mantle convection, *Earth Planet. Sci. Lett.*, *205*,
623 107–121, 2003.
- 624 Bercovici, D., and S. Karato, Theoretical analysis of shear localization in the lithosphere, *Rev. Mineral.*
625 *Geochem.*, *51*, 387–421, 2003.
- 626 Bercovici, D., G. Schubert, and G. A. Glatzmaier, Three-dimensional, infinite Prandtl number,
627 compressible convection in a basally heated spherical shell, *J. Fluid Mech.*, *239*, 683–719,
628 1992.
- 629 Bercovici, D., Y. Ricard, and M. A. Richards, The relation between mantle dynamics and plate
630 tectonics: A primer, in *The History and Dynamics of Global Plate Motions*, edited by M. A.
631 Richards, R. G. Gordon, and R. D. van der Hilst, pp. 5–46, American Geophysical Union, 2000.
- 632 Bleeker, W., The late Archean record: A puzzle in *ca.* 35 pieces, *Lithos*, *71*, 99–134, 2003.
- 633 Bradley, D. C., Passive margins through earth history, *Earth-Sci. Rev.*, *91*, 1–26, 2008.
- 634 Busse, F. H., On the stability of two-dimensional convection in a layer heated from below, *J. Math.*
635 *Phys.*, *46*, 140–150, 1967.
- 636 Byerlee, J., Friction of rocks, *PAGEOPH*, *116*, 615–626, 1978.
- 637 Christensen, U., Convection with pressure- and temperature-dependent non-Newtonian rheology,
638 *Geophys. J. R. Astron. Soc.*, *77*, 343–384, 1984.
- 639 Christensen, U. R., Thermal evolution models for the Earth, *J. Geophys. Res.*, *90*, 2995–3007, 1985.
- 640 Christensen, U. R., and D. A. Yuen, The interaction of a subducting lithospheric slab with a chemical
641 or phase boundary, *J. Geophys. Res.*, *89*, 4389–4402, 1984.
- 642 Condie, K. C., and V. Pease (Eds.), *When Did Plate Tectonics Begin on Planet Earth?*, Geological
643 Society of America, 2008.
- 644 Conrad, C. P., and B. H. Hager, Effects of plate bending and fault strength at subduction zones on plate
645 dynamics, *J. Geophys. Res.*, *104*, 17,551–17,571, 1999.

- 646 Crisp, J. A., Rates of magma emplacement and volcanic output, *J. Volcanol. Geotherm. Res.*, *20*,
647 177–211, 1984.
- 648 Daly, S. F., Convection with decaying heat sources: constant viscosity, *Geophys. J. R. Astron. Soc.*, *61*,
649 519–547, 1980.
- 650 Davies, G. F., Effect of plate bending on the Urey ratio and the thermal evolution of the mantle, *Earth*
651 *Planet. Sci. Lett.*, *287*, 513–518, 2009.
- 652 Deschamps, F., P. J. Tackley, and T. Nakagawa, Temperature and heat flux scalings for isoviscous
653 thermal convection in spherical geometry, *Geophys. J. Int.*, *182*, 137–154, 2010.
- 654 Evans, R. L., G. Hirth, K. Baba, D. Forsyth, A. Chave, and R. Mackie, Geophysical evidence from the
655 MELT area for compositional controls on oceanic plates, *Nature*, *437*, 249–252, 2005.
- 656 Faul, U. H., and I. Jackson, Diffusion creep of dry, melt-free olivine, *J. Geophys. Res.*, *112*, B04204,
657 doi:10.1029/2006JB004586, 2007.
- 658 Fei, Y., J. Van Orman, J. Li, W. van Westrennen, C. Sanloup, W. Minarik, K. Hirose, T. Komabayashi,
659 M. Walter, and K. Funakoshi, Experimentally determined postspinel transformation boundary
660 in Mg₂SiO₄ using MgO as an internal pressure standard and its geophysical implications, *J.*
661 *Geophys. Res.*, *109*, B02305, doi:10.1029/2003JB002652, 2004.
- 662 Foley, B. J., and T. W. Becker, Generation of plate-like behavior and mantle heterogeneity from
663 a spherical, viscoplastic convection model, *Geochem. Geophys. Geosys.*, *10*, Q08001,
664 doi:10.1029/2009GC002378, 2009.
- 665 Gordon, R. G., and S. Stein, Global tectonics and space geodesy, *Science*, *256*, 333–342, 1992.
- 666 Gurnis, M., S. Zhong, and J. Toth, On the competing roles of fault reactivation and brittle failure in
667 generating plate tectonics from mantle convection, in *The History and Dynamics of Global*
668 *Plate Motions*, edited by M. A. Richards, R. G. Gordon, and R. D. van der Hilst, pp. 73–94,
669 American Geophysical Union, 2000.
- 670 Gurnis, M., C. Hall, and L. Lavier, Evolving force balance during incipient subduction, *Geochem.*
671 *Geophys. Geosys.*, *5*, Q07001, doi:10.1029/2003GC000681, 2004.
- 672 Hager, B. H., Subducted slabs and the geoid: Constraints on mantle rheology and flow, *J. Geophys.*
673 *Res.*, *89*, 6003–6015, 1984.

- 674 Hager, B. H., Mantle viscosity: A comparison of models from postglacial rebound and from the
675 geoid, plate driving forces, and advected heat flux, in *Glacial Isostasy, Sea-Level and Mantle*
676 *Rheology*, edited by R. Sabadini, K. Lambeck, and E. Boschi, pp. 493–513, Kluwer Academic,
677 Dordrecht, 1991.
- 678 Harrison, T. M., The Hadean crust: Evidence from >4 Ga zircon, *Annu. Rev. Earth Planet. Sci.*, 37,
679 479–505, 2009.
- 680 Harrison, T. M., J. Blichert-Toft, W. Müller, F. Albarede, P. Holden, and S. J. Mojzsis, Heterogeneous
681 Hadean hafnium: Evidence of continental crust at 4.4 to 4.5 Ga, *Science*, 310, 1947–1950,
682 2005.
- 683 Herzberg, C., P. D. Asimow, N. Arndt, Y. Niu, C. M. Leshner, J. G. Fitton, M. J. Cheadle, and A. D.
684 Saunders, Temperatures in ambient mantle and plumes: Constraints from basalts, picrites, and
685 komatiites, *Geochem. Geophys. Geosys.*, 8, Q02206, doi:10.1029/2006GC001390, 2007.
- 686 Herzberg, C., K. Condie, and J. Korenaga, Thermal evolution of the Earth and its petrological
687 expression, *Earth Planet. Sci. Lett.*, 292, 79–88, 2010.
- 688 Hirth, G., and D. L. Kohlstedt, Water in the oceanic mantle: Implications for rheology, melt extraction,
689 and the evolution of the lithosphere, *Earth and Planetary Science Letters*, 144, 93–108, 1996.
- 690 Howard, L. N., Convection at high Rayleigh number, in *Proceedings of the Eleventh International*
691 *Congress of Applied Mechanics*, edited by H. Gortler, pp. 1109–1115, Springer-Verlag, New
692 York, 1966.
- 693 Jarvis, G. T., and D. P. McKenzie, Convection in a compressible fluid with infinite Prandtl number, *J.*
694 *Fluid Mech.*, 96, 515–583, 1980.
- 695 Karato, S., *Deformation of Earth Materials: Introduction to the Rheology of the Solid Earth*,
696 Cambridge, New York, 2008.
- 697 Karato, S., and P. Wu, Rheology of the upper mantle: A synthesis, *Science*, 260, 771–778, 1993.
- 698 Karato, S., M. S. Paterson, and J. D. FitzGerald, Rheology of synthetic olivine aggregates: Influence of
699 grain size and water, *J. Geophys. Res.*, 91, 8151–8176, 1986.
- 700 Katsura, T., H. Yamada, T. Shinmei, A. Kubo, S. Ono, M. Kanzaki, A. Yoneda, M. J. Walter, E. Ito,

- 701 S. Urakawa, K. Funakoshi, and W. Utsumi, Post-spinel transition in Mg_2SiO_4 determined by
702 high $P - T$ in situ X-ray deffractometry, *Phys. Earth Planet. Inter.*, *136*, 11–24, 2003.
- 703 Kido, M., and O. Cadec, Inferences of viscosity from the oceanic geoid: Indication of a low viscosity
704 zone below the 660-km discontinuity, *Earth Planet. Sci. Lett.*, *151*, 125–137, 1997.
- 705 King, S. D., Models of mantle viscosity, in *Global Earth Physics: A Handbook of Physical Constants*,
706 pp. 227–236, American Geophysical Union, 1995.
- 707 Korenaga, J., Energetics of mantle convection and the fate of fossil heat, *Geophys. Res. Lett.*, *30*, 1437,
708 doi:10.1029/2003GL016982, 2003.
- 709 Korenaga, J., Archean geodynamics and the thermal evolution of Earth, in *Archean Geodynamics
710 and Environments*, edited by K. Benn, J.-C. Mareschal, and K. Condie, pp. 7–32, American
711 Geophysical Union, Washington, D.C., 2006.
- 712 Korenaga, J., Thermal cracking and the deep hydration of oceanic lithosphere: A key to the generation
713 of plate tectonics?, *J. Geophys. Res.*, *112*, B05408, doi:10.1029/2006JB004502, 2007.
- 714 Korenaga, J., Urey ratio and the structure and evolution of Earth's mantle, *Rev. Geophys.*, *46*, RG2007,
715 doi:10.1029/2007RG000241, 2008a.
- 716 Korenaga, J., Plate tectonics, flood basalts, and the evolution of Earth's oceans, *Terra Nova*, *20*,
717 419–439, 2008b.
- 718 Korenaga, J., Scaling of stagnant-lid convection with Arrhenius rheology and the effects of mantle
719 melting, *Geophys. J. Int.*, *179*, 154–170, 2009.
- 720 Korenaga, J., and T. H. Jordan, Physics of multiscale convection in Earth's mantle: Onset of
721 sublithospheric convection, *J. Geophys. Res.*, *108*, 2333, doi:10.1029/2002JB001760, 2003.
- 722 Korenaga, J., and S. Karato, A new analysis of experimental data on olivine rheology, *J. Geophys. Res.*,
723 *113*, B02403, doi:10.1029/2007JB005100, 2008.
- 724 Korenaga, J., P. B. Kelemen, and W. S. Holbrook, Methods for resolving the origin of large igneous
725 provinces from crustal seismology, *J. Geophys. Res.*, *107*, 2178, doi:10.1029/2001JB001030,
726 2002.
- 727 Landuyt, W., and D. Bercovici, Variations in planetary convection via the effect of climate on damage,
728 *Earth Planet. Sci. Lett.*, *277*, 29–37, 2009.

- 729 Landuyt, W., D. Bercovici, and Y. Ricard, Plate generation and two-phase damage theory in a model of
730 mantle convection, *Geophys. J. Int.*, *174*, 1065–1080, 2008.
- 731 Lenardic, A., F. Nimmo, and L. Moresi, Growth of the hemispheric dichotomy and the cessation of
732 plate tectonics on Mars, *J. Geophys. Res.*, *109*, E02003, doi:10.1029/2003JE002172, 2004.
- 733 McKenzie, D. P., J. M. Roberts, and N. O. Weiss, Convection in the earth's mantle: towards a numerical
734 simulation, *J. Fluid Mech.*, *62*, 465–538, 1974.
- 735 Mei, S., and D. L. Kohlstedt, Influence of water on plastic deformation of olivine aggregates, 1,
736 diffusion creep regime, *J. Geophys. Res.*, *105*, 21,457–21,469, 2000a.
- 737 Mei, S., and D. L. Kohlstedt, Influence of water on plastic deformation of olivine aggregates, 2,
738 dislocation creep regime, *J. Geophys. Res.*, *105*, 21,471–21,481, 2000b.
- 739 Mojzsis, S. J., T. M. Harrison, and R. T. Pidgeon, Oxygen-isotope evidence from ancient zircons for
740 liquid water at the Earth's surface 4,300 Myr ago, *Nature*, *409*, 178–181, 2001.
- 741 Moresi, L., and V. Solomatov, Mantle convection with a brittle lithosphere: thoughts on the global
742 tectonic styles of the Earth and Venus, *Geophys. J. Int.*, *133*, 669–682, 1998.
- 743 Ogawa, M., Plate-like regime of a numerically modeled thermal convection in a fluid with
744 temperature-, pressure-, and stress-history-dependent viscosity, *J. Geophys. Res.*, *108*, 2067,
745 doi:10.1029/2000JB000069, 2003.
- 746 O'Neill, C., and A. Lenardic, Geological consequences of super-sized Earths, *Geophys. Res. Lett.*, *34*,
747 L19204, doi:10.1029/2007GL030598, 2007.
- 748 O'Neill, C., A. Lenardic, L. Moresi, T. H. Torsvik, and C.-T. Lee, Episodic Precambrian subduction,
749 *Earth Planet. Sci. Lett.*, *262*, 552–562, 2007.
- 750 Oxburgh, E. R., and E. M. Parmentier, Compositional and density stratification in oceanic lithosphere -
751 causes and consequences, *J. Geol. Soc. London*, *133*, 343–355, 1977.
- 752 Richards, M. A., W.-S. Yang, J. R. Baumgardner, and H.-P. Bunge, Role of a low-viscosity zone
753 in stabilizing plate tectonics: Implications for comparative terrestrial planetology, *Geochem.*
754 *Geophys. Geosys.*, *2*, 2000GC000,115, 2001.
- 755 Ringwood, A. E., and T. Irifune, Nature of the 650-km seismic discontinuity - implications for mantle
756 dynamics and differentiation, *Nature*, *331*, 131–136, 1988.

- 757 Schubert, G., D. L. Turcotte, and P. Olson, *Mantle Convection in the Earth and Planets*, Cambridge,
758 New York, 2001.
- 759 Soldati, G., L. Boschi, F. Deschamps, and D. Giardini, Inferring radial models of mantle viscosity from
760 gravity (GRACE) data and an evolutionary algorithm, *Phys. Earth Planet. Inter.*, *176*, 19–32,
761 2009.
- 762 Solheim, L. P., and W. R. Peltier, Avalanche effects in phase transition modulated thermal convection,
763 *J. Geophys. Res.*, *99*, 6997–7018, 1994.
- 764 Solomatov, V. S., Can hotter mantle have a larger viscosity?, *Geophys. Res. Lett.*, *23*, 937–940, 1996.
- 765 Solomatov, V. S., Initiation of subduction by small-scale convection, *J. Geophys. Res.*, *109*, B01412,
766 doi:10.1029/2003JB002628, 2004.
- 767 Solomatov, V. S., and L.-N. Moresi, Scaling of time-dependent stagnant lid convection: Application
768 to small-scale convection on earth and other terrestrial planets, *J. Geophys. Res.*, *105*,
769 21,795–21,817, 2000.
- 770 Stein, C., J. Schmalzl, and U. Hansen, The effect of rheological parameters on plate behavior in a
771 self-consistent model of mantle convection, *Phys. Earth Planet. Inter.*, *142*, 225–255, 2004.
- 772 Stern, R. J., Evidence from ophiolites, blueschists, and ultrahigh-pressure metamorphic terranes that the
773 modern episode of subduction tectonics began in Neoproterozoic time, *Geology*, *33*, 557–560,
774 2005.
- 775 Tackley, P. J., Self-consistent generation of tectonic plates in time-dependent, three-dimensional mantle
776 convection simulations, 2. strain weakening and asthenosphere, *Geochem. Geophys. Geosys.*, *1*,
777 2000GC000,043, 2000.
- 778 Tackley, P. J., D. J. Stevenson, G. A. Glatzmaier, and G. Schubert, Effects of an endothermic phase
779 transition at 670 km depth in a spherical model of convection in the Earth's mantle, *Nature*,
780 *361*, 699–704, 1993.
- 781 van Heck, H. J., and P. J. Tackley, Planforms of self-consistently generated plates in 3D spherical
782 geometry, *Geophys. Res. Lett.*, *35*, L19312, doi:10.1029/2008GL035190, 2008.
- 783 Van Kranendonk, M. J., R. H. Smithies, A. H. Hickman, and D. Champion, Review: secular tectonic

784 evolution of Archean continental crust: interplay between horizontal and vertical processes in
785 the formation of the Pilbara Craton, Australia, *Terra Nova*, *19*, 1–38, 2007.

786 Weinstein, S. A., and P. L. Olson, Thermal convection with non-Newtonian plates, *Geophys. J. Int.*,
787 *111*, 515–530, 1992.

788 Yuen, D. A., D. M. Reuteler, S. Balachandar, V. Steinbach, A. V. Malevsky, and J. J. Smedsmo, Various
789 influences on three-dimensional mantle convection with phase transitions, *Phys. Earth Planet.*
790 *Inter.*, *86*, 185–203, 1994.

791 Zhong, S., and M. Gurnis, Role of plates and temperature-dependent viscosity in phase change
792 dynamics, *J. Geophys. Res.*, *99*, 15,903–15,917, 1994.

793 Jun Korenaga, Department of Geology and Geophysics, P.O. Box, 208109, Yale University,
794 New Haven, CT 06520-8109. (jun.korenaga@yale.edu)

795 Received _____

Submitted to *Journal of Geophysical Research*, April 2010; Revised, July 2010; accepted, August 2010.

796 This manuscript was prepared with AGU's \LaTeX macros v5, with the extension package
797 'AGU++' by P. W. Daly, version 1.6b from 1999/08/19.

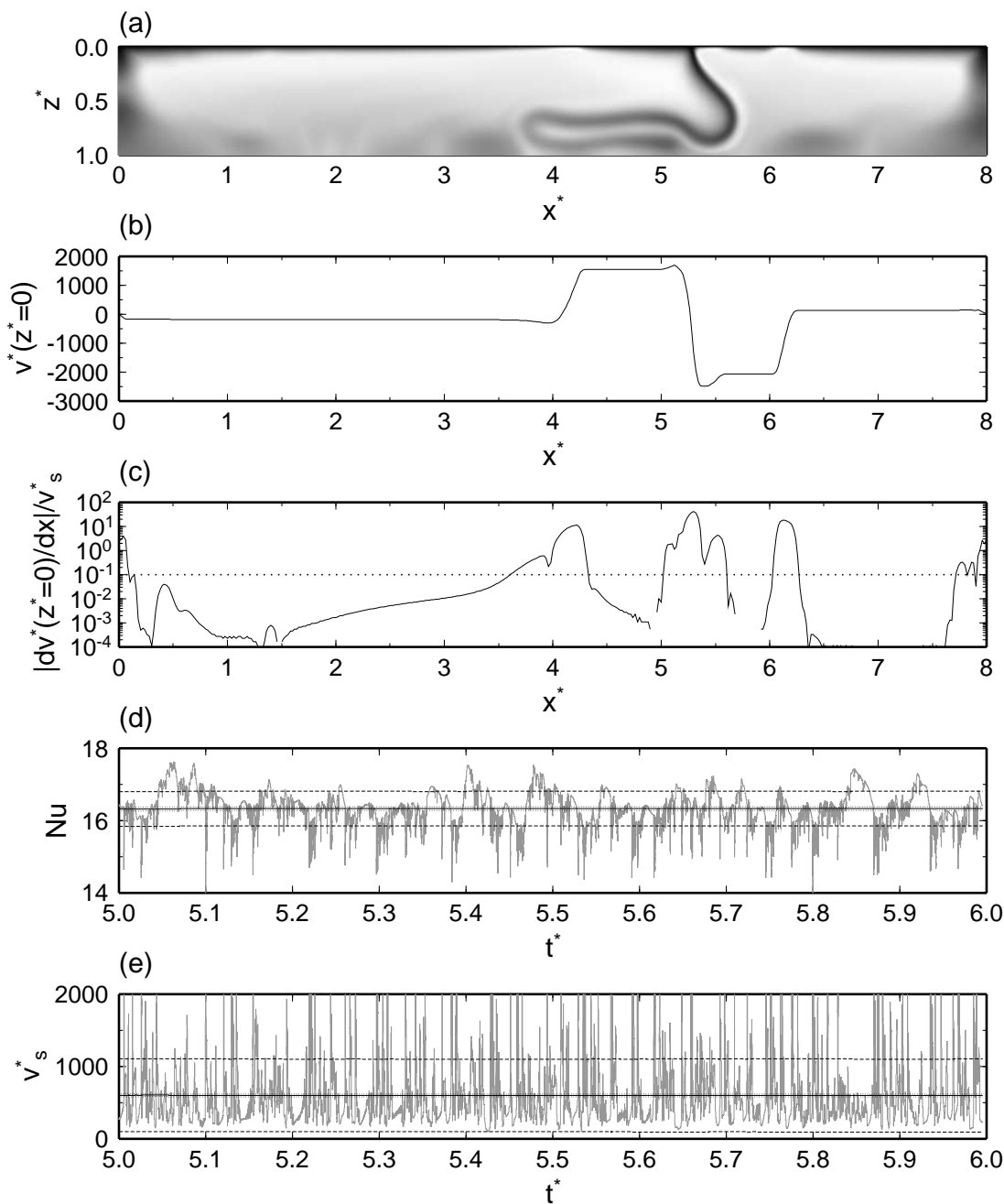
798 **Figure Captions**

Figure 1. Example of simulation results from the case of $\gamma=0.6$, $\theta_0=15$, and $H^*=20$ with the standard pseudoplastic rheology [equation (12)]. (a) Snapshot of the temperature field. Darker shading corresponds to lower temperature. (b) Surface velocity profile and (c) horizontal strain rate scaled by by the average surface velocity, corresponding to the snapshot shown in (a). $P_{0.1}$ is 0.76 for this particular velocity profile, i.e., 76% of the surface has the scaled strain rate lower than 0.1 (shown by dotted in (c)). (d) Nusselt number and (e) root-mean-square surface velocity as a function of time (shown in gray). For this model run, statistically steady state was achieved at $t^* = 1.8$, and running average is taken from the subsequent model results. In (d) and (e), the running average and its uncertainty (1σ) is shown as solid and dotted lines, respectively, and the one standard deviation of the temporal variation itself is shown by dashed line.

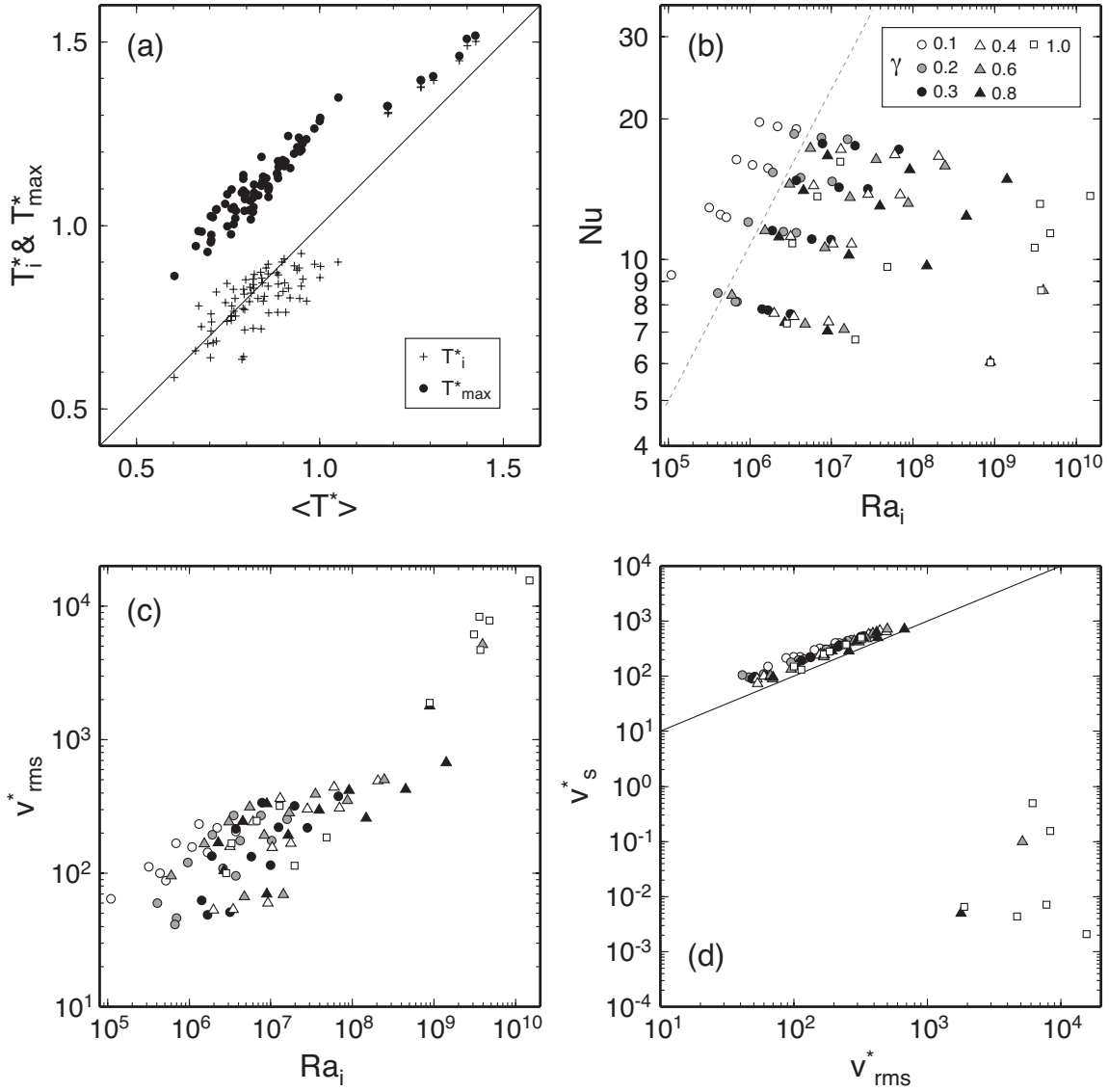


Figure 2. Correlations among convection diagnostics from reference runs. (a) Internal temperature T_i^* (cross) and maximum temperature T_{\max}^* (solid circle) are compared with domain-average temperature $\langle T^* \rangle$. (b) Nu and Ra_i . Dashed line indicates the slope of $Ra_i^{1/3}$. (c) v_{rms}^* and Ra_i . (d) v_s^* and v_{rms}^* . In (b)-(d), different symbols denote runs with different γ , as shown by the legend in (b).

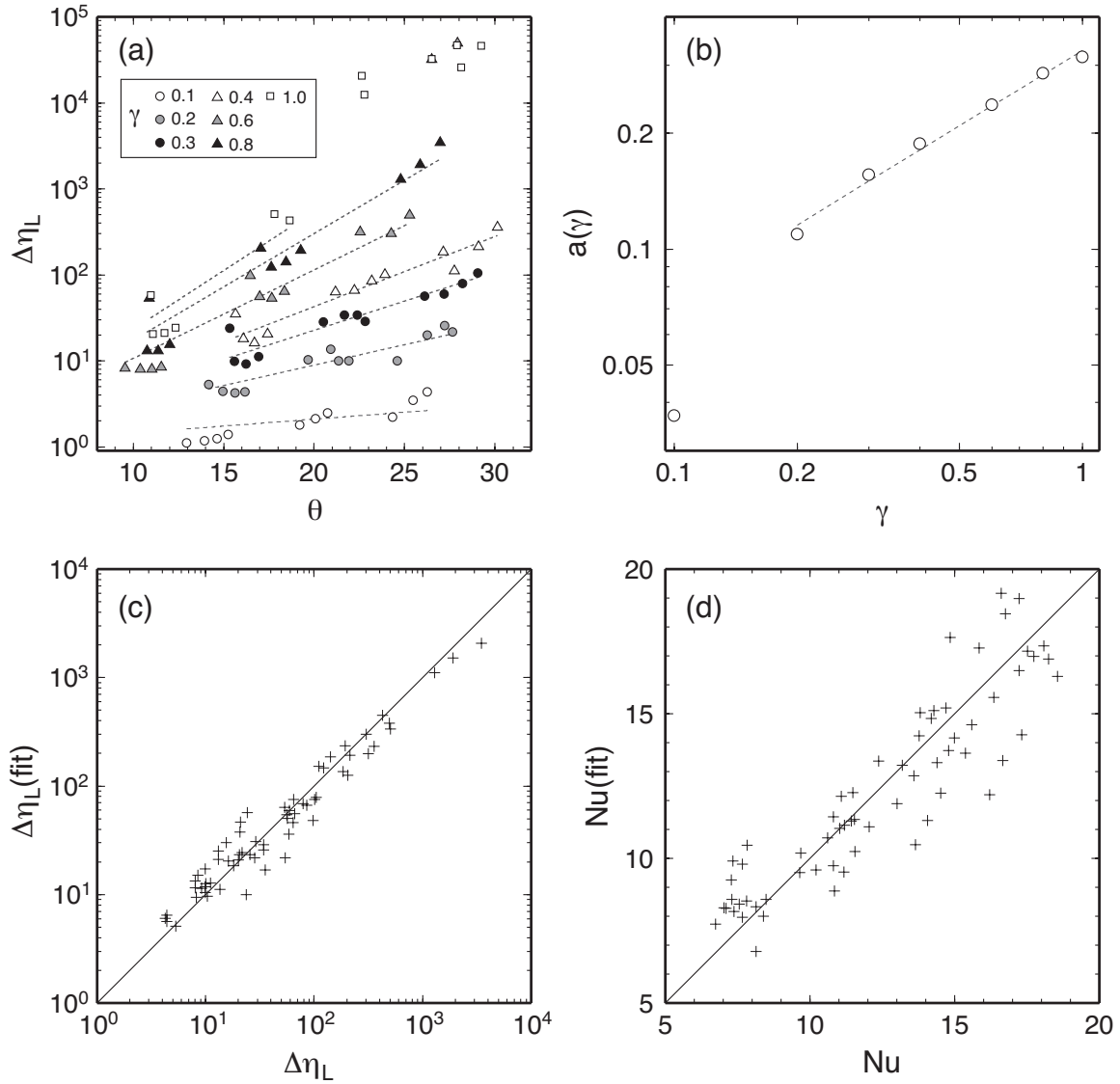


Figure 3. The systematics of reference runs can be summarized through effective lithospheric viscosity contrast $\Delta\eta_L$. (a) $\Delta\eta_L$ as a function of θ . Different symbols denote runs with different γ , and dashed lines are fitted trend in the form of equation (37) for each γ . Data with $\Delta\eta_L$ greater than 10^4 are stagnant-lid runs, which are excluded from linear regression. (b) The fitted coefficient a as a function of γ . Dashed line represents equation (38). (c) Comparison of measured $\Delta\eta_L$ with predicted values based on equations (37) and (38). (d) Comparison of measured Nu with predicted values based on equation (35).

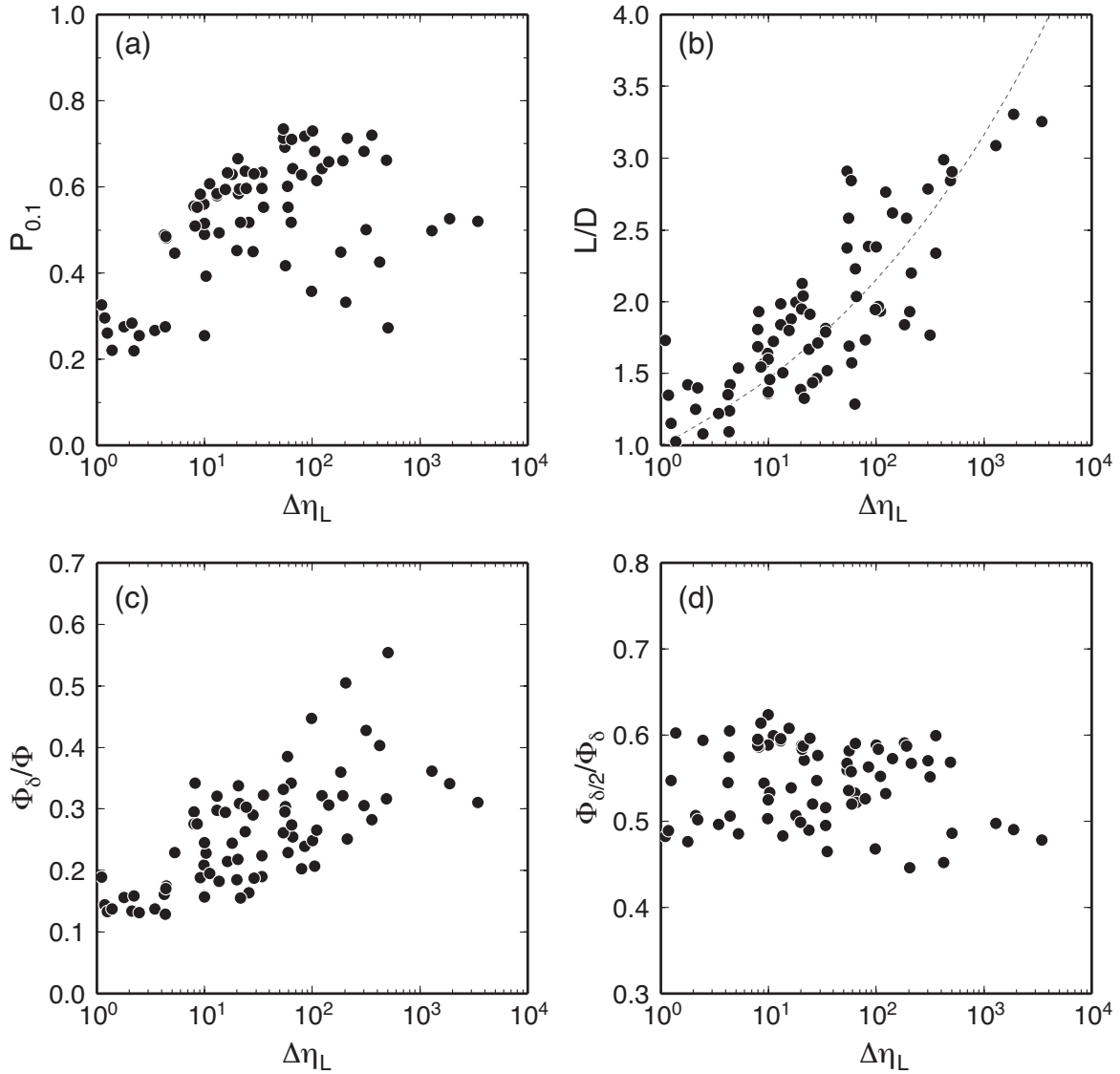


Figure 4. Covariations of measured lithospheric viscosity contrast $\Delta\eta_L$ with (a) plateness $P_{0.1}$, (b) the average aspect ratio of convection cells L/D , (c) the fraction of viscous dissipation taking place in the top thermal boundary layer with respect to that in the entire domain Φ_δ/Φ , and (d) the fraction of viscous dissipation in the upper half of the boundary layer with respect to that in the entire boundary layer $\Phi_{\delta/2}/\Phi_\delta$. Dashed line in (b) corresponds to $L/D = \Delta\eta_L^{1/6}$.

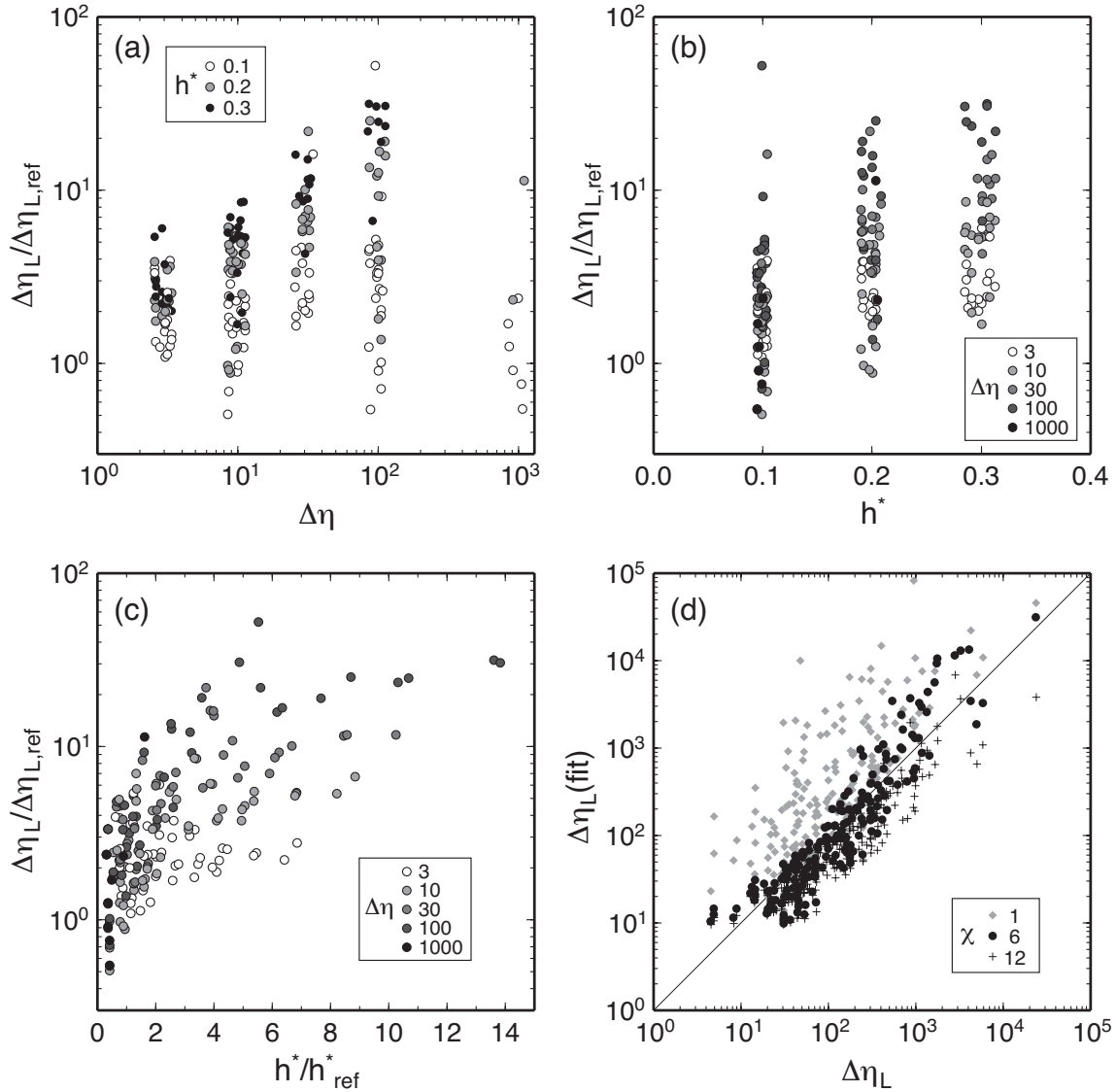


Figure 5. The effect of additional depth-dependent viscosity on the lithospheric viscosity contrast. The deviation from the prediction based on standard pseudoplastic rheology, $\Delta\eta_L/\Delta\eta_{L,ref}$, is shown as a function of (a) the viscosity contrast due to dehydration $\Delta\eta$, (b) the thickness of dehydrated layer h^* , and (c) the same thickness but scaled by the reference thickness, h^*/h^*_{ref} . Different symbols denote different h^* in (a) and different $\Delta\eta$ in (b) and (c). Note that in (a) and (b) the values of $\Delta\eta$ and h^* are slightly perturbed randomly for display purposes. (d) Comparison of measured $\Delta\eta_L$ with predicted values based on equation (44), for three different values of χ .

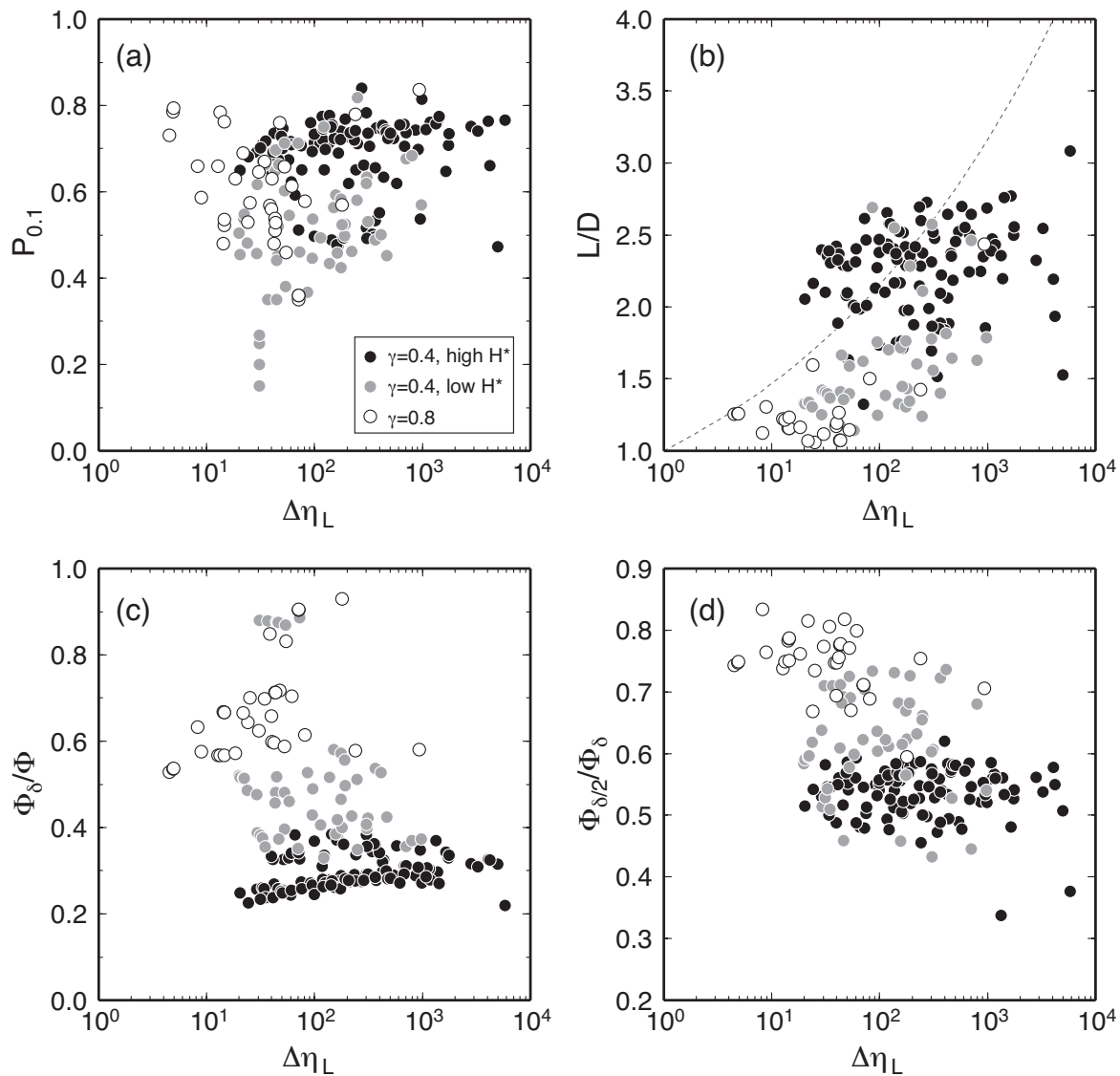


Figure 6. Same as Figure 4 but for runs with shallow stiffening. Different symbols correspond to different groups of runs: γ of 0.4 with high H^* (solid circle; Tables A3-A5), γ of 0.4 with low H^* (gray circle; Tables A6-A7), and γ of 0.8 (open circle; Table A8).

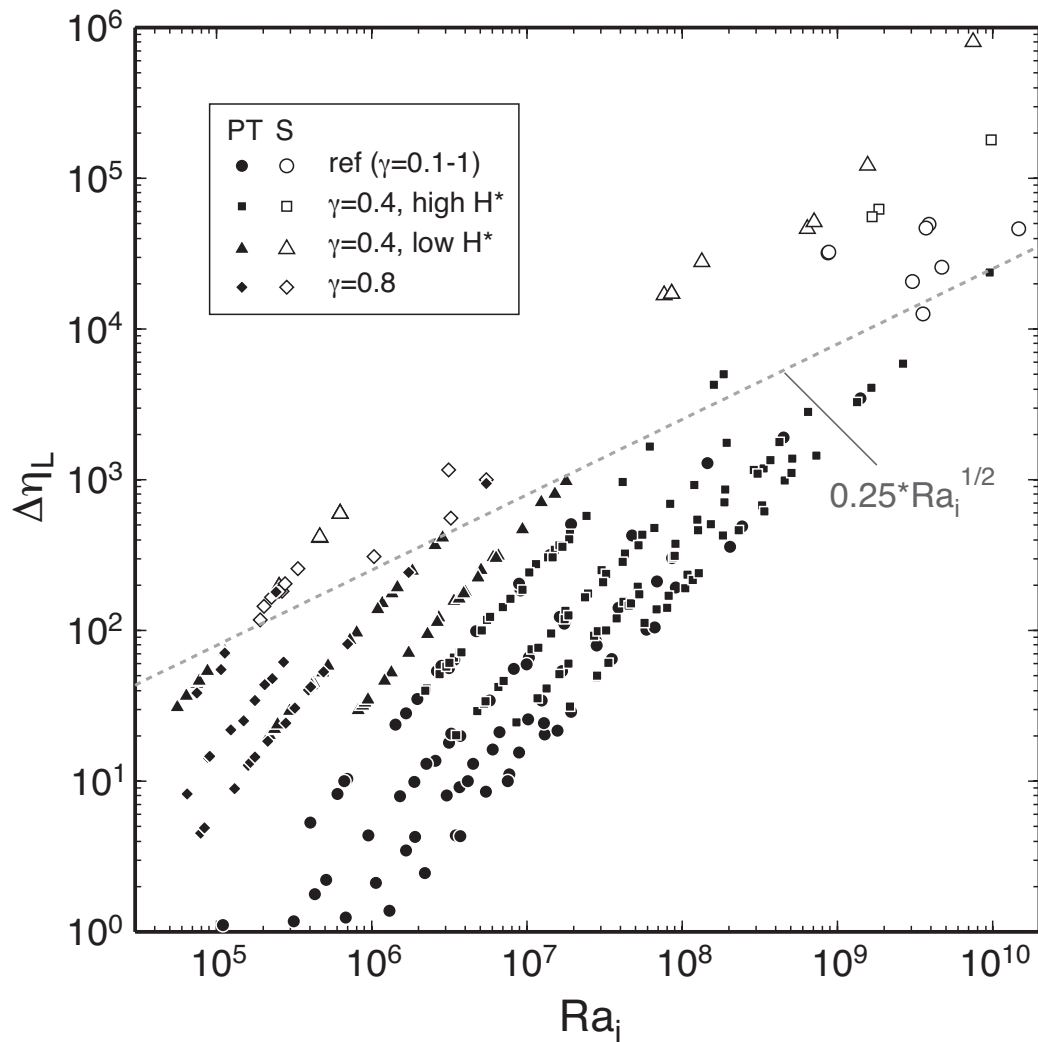


Figure 7. Covariation of Ra_i and $\Delta\eta_L$ for all model runs. Solid and open symbols denote plate-tectonic and stagnant-lid runs, respectively. Dashed line represents an approximate divide between these two modes of convection ($\Delta\eta_L \sim 0.25 Ra_i^{1/2}$).

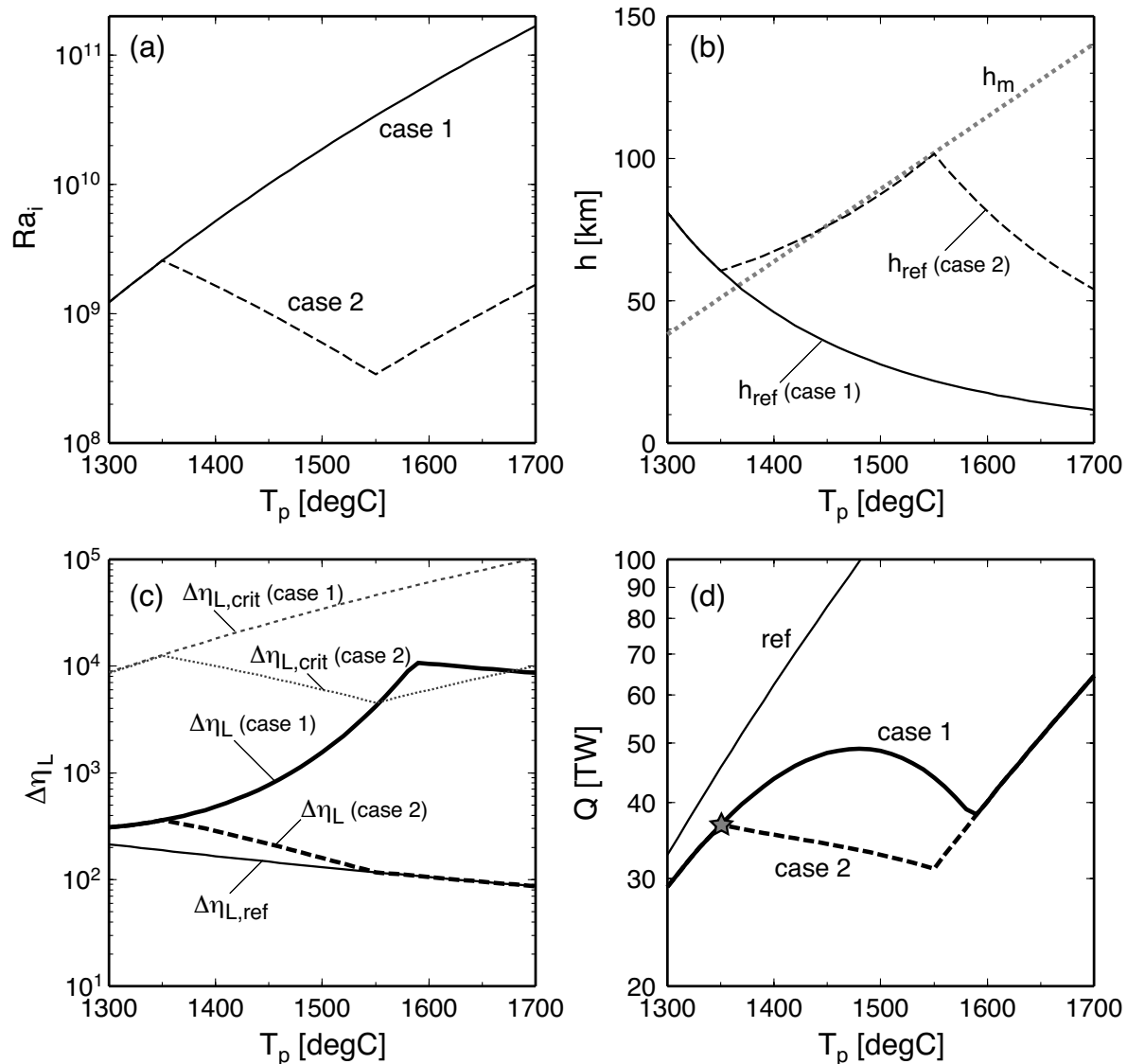


Figure 8. A worked example of how the new scaling laws of plate-tectonic convection may be used to build heat-flow scaling for Earth. (a) Internal Rayleigh number Ra_i as a function of mantle potential temperature T_p . (b) Thicknesses of dehydrated lithosphere (h_m , dotted) and reference thermal boundary layer (h_{ref} , solid for case 1 and dashed for case 2) [equation (42)]. (c) Lithospheric viscosity contrast for case 1 (thick solid), case 2 (thick dashed), and a reference case with no effect of mantle melting, i.e., $h_m^* = 0$ (thin solid). Also shown are the critical viscosity contrast for plate-tectonic convection (dashed for case 1 and dotted for case 2). (d) Relation between T_p and surface heat flux Q . Legend is the same as in (c). Star denotes convective heat flux at the present day (38 TW at 1350°C). See the main text for details.

799 **Tables****Table A1.** Numerical results for reference runs ($\gamma < 0.5$)

γ	θ_0	H^*	T_{\max}^*	T_i^*	$\langle T^* \rangle$	Nu	θ	Ra_i	v_{rms}^*	v_s^*	$P_{0.1}$	Φ	Φ_δ/Φ
0.1	15	8	0.86	0.59	0.60	9.27	12.9	1.10×10^5	6.40×10^1	1.49×10^2	0.33	2.73×10^7	0.19
0.1	15	12	0.93	0.68	0.69	12.93	13.9	3.18×10^5	1.12×10^2	2.26×10^2	0.30	4.25×10^7	0.14
0.1	15	16	0.98	0.75	0.76	16.39	14.6	6.85×10^5	1.68×10^2	3.10×10^2	0.26	5.77×10^7	0.13
0.1	15	20	1.02	0.82	0.81	19.67	15.3	1.32×10^6	2.33×10^2	3.97×10^2	0.22	7.31×10^7	0.14
0.1	20	12	0.96	0.71	0.70	12.50	19.2	4.36×10^5	1.00×10^2	2.22×10^2	0.27	4.22×10^7	0.16
0.1	20	16	1.00	0.77	0.77	15.95	20.1	1.08×10^6	1.57×10^2	3.18×10^2	0.28	5.77×10^7	0.13
0.1	20	20	1.04	0.84	0.82	19.28	20.8	2.21×10^6	2.19×10^2	4.02×10^2	0.25	7.30×10^7	0.13
0.1	25	12	0.97	0.74	0.70	12.32	24.4	5.15×10^5	8.78×10^1	2.13×10^2	0.22	4.19×10^7	0.16
0.1	25	16	1.02	0.80	0.77	15.69	25.5	1.68×10^6	1.43×10^2	3.01×10^2	0.27	5.73×10^7	0.14
0.1	25	20	1.05	0.85	0.82	19.04	26.3	3.74×10^6	2.06×10^2	3.97×10^2	0.28	7.28×10^7	0.13
0.2	15	8	0.94	0.66	0.66	8.48	14.2	4.05×10^5	5.97×10^1	1.11×10^2	0.45	2.67×10^7	0.23
0.2	15	12	1.00	0.74	0.75	12.04	15.0	9.57×10^5	1.21×10^2	2.06×10^2	0.48	4.20×10^7	0.17
0.2	15	16	1.04	0.79	0.81	15.37	15.6	1.93×10^6	1.94×10^2	3.20×10^2	0.49	5.75×10^7	0.16
0.2	15	20	1.08	0.83	0.86	18.55	16.2	3.49×10^6	2.72×10^2	4.26×10^2	0.48	7.30×10^7	0.17
0.2	20	8	0.98	0.72	0.68	8.14	19.7	6.97×10^5	4.61×10^1	9.66×10^1	0.39	2.62×10^7	0.23
0.2	20	12	1.05	0.78	0.76	11.49	20.9	2.58×10^6	1.08×10^2	1.99×10^2	0.49	4.17×10^7	0.18
0.2	20	16	1.07	0.83	0.81	14.98	21.4	4.18×10^6	1.76×10^2	3.06×10^2	0.49	5.72×10^7	0.16
0.2	20	20	1.10	0.87	0.86	18.24	21.9	7.57×10^6	2.70×10^2	4.57×10^2	0.52	7.28×10^7	0.16
0.2	25	8	0.98	0.78	0.67	8.13	24.6	6.69×10^5	4.13×10^1	1.06×10^2	0.25	2.58×10^7	0.25
0.2	25	12	1.05	0.83	0.77	11.43	26.3	3.73×10^6	9.51×10^1	1.82×10^2	0.45	4.11×10^7	0.18
0.2	25	16	1.09	0.87	0.82	14.69	27.2	1.02×10^7	1.76×10^2	3.10×10^2	0.52	5.64×10^7	0.16
0.2	25	20	1.11	0.90	0.86	18.08	27.7	1.59×10^7	2.53×10^2	4.34×10^2	0.52	7.18×10^7	0.16
0.3	15	8	1.02	0.68	0.71	7.83	15.3	1.43×10^6	6.27×10^1	1.02×10^2	0.64	2.65×10^7	0.26
0.3	15	12	1.04	0.75	0.77	11.54	15.6	1.90×10^6	1.35×10^2	2.19×10^2	0.56	4.20×10^7	0.21
0.3	15	16	1.08	0.80	0.83	14.79	16.2	3.70×10^6	2.15×10^2	3.44×10^2	0.58	5.75×10^7	0.19
0.3	15	20	1.13	0.84	0.89	17.73	16.9	7.76×10^6	3.38×10^2	5.42×10^2	0.61	7.30×10^7	0.20
0.3	20	8	1.02	0.76	0.70	7.81	20.5	1.68×10^6	4.90×10^1	8.94×10^1	0.45	2.61×10^7	0.29
0.3	20	12	1.08	0.81	0.79	11.08	21.7	5.80×10^6	1.34×10^2	2.23×10^2	0.60	4.14×10^7	0.22
0.3	20	16	1.12	0.84	0.84	14.29	22.4	1.25×10^7	2.20×10^2	3.65×10^2	0.63	5.71×10^7	0.19
0.3	20	20	1.14	0.87	0.88	17.53	22.8	1.94×10^7	3.20×10^2	5.26×10^2	0.63	7.27×10^7	0.19
0.3	25	8	1.04	0.82	0.72	7.66	26.1	3.17×10^6	5.10×10^1	9.93×10^1	0.42	2.54×10^7	0.30
0.3	25	12	1.09	0.85	0.80	11.03	27.2	9.97×10^6	1.15×10^2	1.91×10^2	0.55	4.05×10^7	0.23
0.3	25	16	1.13	0.88	0.85	14.18	28.2	2.82×10^7	2.19×10^2	3.49×10^2	0.63	5.55×10^7	0.20
0.3	25	20	1.16	0.91	0.90	17.22	29.1	6.71×10^7	3.76×10^2	5.84×10^2	0.68	7.08×10^7	0.21
0.4	15	8	1.04	0.68	0.72	7.67	15.6	1.99×10^6	5.32×10^1	8.93×10^1	0.55	2.66×10^7	0.32
0.4	15	12	1.07	0.77	0.80	11.20	16.1	3.18×10^6	1.59×10^2	2.50×10^2	0.63	4.19×10^7	0.24
0.4	15	16	1.11	0.81	0.85	14.39	16.7	6.03×10^6	2.43×10^2	3.89×10^2	0.63	5.74×10^7	0.21
0.4	15	20	1.16	0.84	0.90	17.23	17.4	1.31×10^7	3.63×10^2	5.79×10^2	0.67	7.31×10^7	0.22
0.4	20	8	1.06	0.79	0.74	7.56	21.2	3.43×10^6	5.36×10^1	7.34×10^1	0.52	2.57×10^7	0.34
0.4	20	12	1.11	0.83	0.82	10.80	22.2	1.04×10^7	1.56×10^2	2.38×10^2	0.64	4.13×10^7	0.25
0.4	20	16	1.16	0.86	0.89	13.81	23.2	2.81×10^7	3.03×10^2	4.55×10^2	0.72	5.71×10^7	0.24
0.4	20	20	1.20	0.89	0.93	16.75	23.9	5.92×10^7	4.43×10^2	6.68×10^2	0.73	7.25×10^7	0.25
0.4	25	8	1.09	0.84	0.75	7.37	27.1	9.21×10^6	5.96×10^1	1.00×10^2	0.45	2.52×10^7	0.36
0.4	25	12	1.11	0.87	0.84	10.81	27.8	1.75×10^7	1.67×10^2	2.26×10^2	0.61	3.92×10^7	0.27
0.4	25	16	1.16	0.90	0.90	13.76	29.1	6.93×10^7	3.08×10^2	4.16×10^2	0.71	5.44×10^7	0.25
0.4	25	20	1.21	0.92	0.95	16.61	30.1	2.05×10^8	4.94×10^2	6.45×10^2	0.72	6.88×10^7	0.28

Table A2. Numerical results for reference runs ($\gamma > 0.5$)

γ	θ_0	H^*	T_{\max}^*	T_i^*	$\langle T^* \rangle$	Nu	θ	Ra_i	v_{rms}^*	v_s^*	$P_{0.1}$	Φ	Φ_δ/Φ
0.6	10	8	0.95	0.64	0.70	8.39	9.5	6.05×10^5	9.53×10^1	1.36×10^2	0.51	2.68×10^7	0.34
0.6	10	12	1.04	0.71	0.79	11.55	10.4	1.54×10^6	1.66×10^2	2.41×10^2	0.56	4.23×10^7	0.29
0.6	10	16	1.10	0.76	0.86	14.52	11.0	3.07×10^6	2.42×10^2	3.56×10^2	0.56	5.78×10^7	0.28
0.6	10	20	1.16	0.80	0.92	17.31	11.6	5.50×10^6	3.15×10^2	4.63×10^2	0.55	7.34×10^7	0.28
0.6	15	8	1.10	0.74	0.76	7.29	16.5	4.76×10^6	6.65×10^1	1.03×10^2	0.36	2.61×10^7	0.45
0.6	15	12	1.13	0.79	0.85	10.60	17.0	8.32×10^6	1.92×10^2	2.90×10^2	0.69	4.17×10^7	0.30
0.6	15	16	1.18	0.82	0.90	13.60	17.7	1.69×10^7	2.84×10^2	4.39×10^2	0.71	5.71×10^7	0.26
0.6	15	20	1.22	0.85	0.95	16.35	18.4	3.52×10^7	3.93×10^2	5.96×10^2	0.71	7.31×10^7	0.27
0.6	20	8	1.13	0.83	0.79	7.10	22.5	1.42×10^7	6.93×10^1	8.92×10^1	0.50	2.54×10^7	0.43
0.6	20	12	1.40	1.38	1.28	8.59	27.9	3.91×10^9	5.16×10^3	9.91×10^{-2}	0.00	3.41×10^7	0.35
0.6	20	16	1.21	0.88	0.94	13.20	24.3	8.69×10^7	3.52×10^2	4.85×10^2	0.68	5.63×10^7	0.31
0.6	20	20	1.26	0.89	0.98	15.85	25.3	2.45×10^8	5.01×10^2	7.14×10^2	0.66	7.19×10^7	0.32
0.8	10	8	1.09	0.64	0.79	7.34	10.9	2.66×10^6	1.05×10^2	1.57×10^2	0.73	2.69×10^7	0.33
0.8	10	12	1.07	0.72	0.82	11.17	10.7	2.28×10^6	1.70×10^2	2.48×10^2	0.58	4.23×10^7	0.32
0.8	10	16	1.14	0.76	0.88	14.06	11.4	4.53×10^6	2.44×10^2	3.64×10^2	0.58	5.78×10^7	0.30
0.8	10	20	1.20	0.80	0.94	16.66	12.0	8.97×10^6	3.30×10^2	5.00×10^2	0.59	7.36×10^7	0.29
0.8	15	8	1.14	0.77	0.79	7.03	17.1	8.92×10^6	7.00×10^1	9.55×10^1	0.33	2.58×10^7	0.50
0.8	15	12	1.18	0.81	0.89	10.22	17.6	1.63×10^7	1.93×10^2	2.89×10^2	0.64	4.13×10^7	0.32
0.8	15	16	1.23	0.84	0.95	13.01	18.5	3.90×10^7	2.98×10^2	4.43×10^2	0.66	5.74×10^7	0.31
0.8	15	20	1.28	0.86	1.00	15.59	19.3	9.11×10^7	4.17×10^2	6.27×10^2	0.66	7.32×10^7	0.32
0.8	20	8	1.32	1.30	1.18	6.04	26.5	8.79×10^8	1.79×10^3	4.93×10^{-3}	0.00	2.06×10^7	0.42
0.8	20	12	1.24	0.88	0.94	9.69	24.8	1.47×10^8	2.59×10^2	2.90×10^2	0.50	4.04×10^7	0.36
0.8	20	16	1.29	0.89	1.00	12.38	25.9	4.51×10^8	4.25×10^2	5.07×10^2	0.53	5.53×10^7	0.34
0.8	20	20	1.35	0.90	1.05	14.84	27.0	1.42×10^9	6.75×10^2	7.17×10^2	0.52	7.15×10^7	0.31
1.0	10	8	1.10	0.64	0.79	7.30	11.0	2.85×10^6	1.00×10^2	1.52×10^2	0.60	2.69×10^7	0.39
1.0	10	12	1.11	0.72	0.84	10.84	11.1	3.29×10^6	1.67×10^2	2.50×10^2	0.58	4.24×10^7	0.34
1.0	10	16	1.17	0.76	0.91	13.64	11.7	6.67×10^6	2.48×10^2	3.80×10^2	0.60	5.80×10^7	0.31
1.0	10	20	1.23	0.79	0.96	16.21	12.3	1.29×10^7	3.21×10^2	5.02×10^2	0.60	7.38×10^7	0.30
1.0	15	8	1.19	0.86	0.84	6.74	17.8	1.94×10^7	1.13×10^2	1.32×10^2	0.27	2.52×10^7	0.55
1.0	15	12	1.24	0.83	0.91	9.65	18.7	4.80×10^7	1.86×10^2	2.79×10^2	0.43	4.14×10^7	0.40
1.0	15	16	1.51	1.49	1.40	10.61	22.6	3.08×10^9	6.13×10^3	4.93×10^{-1}	0.00	4.89×10^7	0.30
1.0	15	20	1.52	1.50	1.42	13.18	22.8	3.58×10^9	8.31×10^3	1.55×10^{-1}	0.00	6.32×10^7	0.29
1.0	20	8	1.33	1.31	1.19	6.04	26.5	8.89×10^8	1.89×10^3	6.51×10^{-3}	0.00	2.07×10^7	0.43
1.0	20	12	1.39	1.38	1.28	8.61	27.9	3.72×10^9	4.71×10^3	4.37×10^{-3}	0.00	3.41×10^7	0.34
1.0	20	16	1.41	1.40	1.31	11.38	28.1	4.76×10^9	7.85×10^3	7.17×10^{-3}	0.00	4.82×10^7	0.31
1.0	20	20	1.46	1.45	1.38	13.69	29.2	1.49×10^{10}	1.57×10^4	2.07×10^{-3}	0.00	6.30×10^7	0.24

Table A3. Numerical results with shallow stiffening ($\gamma = 0.4$, $\theta_0 = 15$, and $H^* > 7$)

θ_0	H^*	h^*	$\Delta\eta$	T_{\max}^*	$\langle T^* \rangle$	Nu	θ	Ra_i	v_{rms}^*	v_s^*	$P_{0.1}$	Φ	Φ_δ/Φ
15	8	0.1	3	1.08	0.73	7.43	16.1	3.38×10^6	6.49×10^1	1.10×10^2	0.59	2.64×10^7	0.38
15	8	0.1	10	1.06	0.75	7.53	15.9	2.74×10^6	6.67×10^1	9.24×10^1	0.71	2.62×10^7	0.33
15	8	0.1	30	1.05	0.75	7.62	15.8	2.28×10^6	7.51×10^1	1.10×10^2	0.69	2.62×10^7	0.33
15	8	0.1	100	1.07	0.75	7.49	16.0	3.01×10^6	7.62×10^1	1.13×10^2	0.67	2.62×10^7	0.33
15	8	0.2	3	1.05	0.76	7.63	15.7	2.22×10^6	9.88×10^1	1.41×10^2	0.65	2.60×10^7	0.33
15	8	0.2	10	1.08	0.79	7.40	16.2	3.69×10^6	1.07×10^2	1.43×10^2	0.71	2.59×10^7	0.33
15	8	0.2	30	1.11	0.82	7.23	16.6	5.57×10^6	1.11×10^2	1.39×10^2	0.78	2.58×10^7	0.31
15	8	0.2	100	1.15	0.87	6.94	17.3	1.15×10^7	1.15×10^2	1.31×10^2	0.84	2.57×10^7	0.28
15	8	0.3	3	1.07	0.77	7.47	16.1	3.18×10^6	9.47×10^1	1.34×10^2	0.62	2.59×10^7	0.34
15	8	0.3	10	1.11	0.81	7.21	16.7	5.80×10^6	1.05×10^2	1.34×10^2	0.65	2.59×10^7	0.34
15	8	0.3	30	1.15	0.85	6.98	17.2	1.03×10^7	1.07×10^2	1.27×10^2	0.65	2.58×10^7	0.34
15	12	0.1	3	1.08	0.80	11.13	16.2	3.50×10^6	1.65×10^2	2.55×10^2	0.65	4.18×10^7	0.25
15	12	0.1	10	1.10	0.82	10.94	16.5	4.77×10^6	1.89×10^2	2.87×10^2	0.69	4.16×10^7	0.26
15	12	0.1	30	1.10	0.83	10.87	16.6	5.29×10^6	1.87×10^2	2.79×10^2	0.71	4.16×10^7	0.26
15	12	0.1	100	1.12	0.85	10.74	16.8	6.54×10^6	1.89×10^2	2.73×10^2	0.74	4.14×10^7	0.27
15	12	0.2	3	1.11	0.83	10.86	16.6	5.42×10^6	1.91×10^2	2.82×10^2	0.67	4.16×10^7	0.26
15	12	0.2	10	1.15	0.88	10.45	17.2	1.07×10^7	1.96×10^2	2.69×10^2	0.71	4.16×10^7	0.27
15	12	0.2	30	1.58	1.43	7.58	23.7	9.82×10^9	8.13×10^3	1.57×10^{-2}	0.00	3.09×10^7	0.36
15	12	0.3	3	1.12	0.84	10.70	16.8	7.07×10^6	1.82×10^2	2.62×10^2	0.68	4.17×10^7	0.26
15	12	0.3	10	1.18	0.90	10.17	17.7	1.78×10^7	1.89×10^2	2.49×10^2	0.71	4.16×10^7	0.27
15	12	0.3	30	1.21	0.93	9.89	18.2	3.03×10^7	1.88×10^2	2.32×10^2	0.71	4.15×10^7	0.29
15	16	0.1	3	1.13	0.87	14.11	17.0	8.58×10^6	2.76×10^2	4.31×10^2	0.68	5.74×10^7	0.23
15	16	0.1	10	1.15	0.89	13.86	17.3	1.18×10^7	2.92×10^2	4.43×10^2	0.72	5.74×10^7	0.24
15	16	0.1	30	1.17	0.91	13.63	17.6	1.62×10^7	2.92×10^2	4.24×10^2	0.75	5.72×10^7	0.25
15	16	0.1	100	1.21	0.95	13.28	18.1	2.70×10^7	4.25×10^2	3.76×10^2	0.76	5.63×10^7	0.27
15	16	0.2	3	1.16	0.89	13.77	17.4	1.34×10^7	2.98×10^2	4.41×10^2	0.69	5.74×10^7	0.24
15	16	0.2	10	1.21	0.94	13.22	18.2	2.87×10^7	3.02×10^2	4.16×10^2	0.71	5.73×10^7	0.26
15	16	0.2	30	1.25	0.97	12.83	18.7	5.15×10^7	2.97×10^2	3.82×10^2	0.73	5.71×10^7	0.28
15	16	0.2	100	1.30	1.02	12.28	19.6	1.25×10^8	3.11×10^2	3.80×10^2	0.72	5.71×10^7	0.29
15	16	0.3	3	1.18	0.91	13.53	17.8	1.86×10^7	2.95×10^2	4.23×10^2	0.72	5.73×10^7	0.24
15	16	0.3	10	1.24	0.96	12.96	18.5	4.21×10^7	2.81×10^2	3.64×10^2	0.74	5.73×10^7	0.27
15	16	0.3	30	1.28	0.99	12.47	19.3	9.10×10^7	2.84×10^2	3.46×10^2	0.75	5.72×10^7	0.28
15	16	0.3	100	1.33	1.03	12.04	20.0	1.89×10^8	2.86×10^2	3.25×10^2	0.74	5.69×10^7	0.29
15	20	0.1	3	1.18	0.93	16.89	17.8	1.89×10^7	3.89×10^2	6.00×10^2	0.70	7.31×10^7	0.23
15	20	0.1	10	1.21	0.95	16.55	18.1	2.79×10^7	3.87×10^2	5.70×10^2	0.73	7.30×10^7	0.25
15	20	0.1	100	1.27	1.00	15.81	19.0	6.82×10^7	3.94×10^2	5.42×10^2	0.78	7.29×10^7	0.28
15	20	0.2	3	1.21	0.95	16.53	18.2	2.85×10^7	3.93×10^2	5.73×10^2	0.70	7.31×10^7	0.25
15	20	0.2	10	1.25	0.99	15.96	18.8	5.70×10^7	3.99×10^2	5.35×10^2	0.71	7.30×10^7	0.27
15	20	0.2	30	1.30	1.02	15.45	19.4	1.08×10^8	3.99×10^2	5.12×10^2	0.72	7.29×10^7	0.28
15	20	0.3	3	1.22	0.96	16.40	18.3	3.34×10^7	3.80×10^2	5.36×10^2	0.71	7.30×10^7	0.25
15	20	0.3	10	1.28	1.01	15.67	19.2	8.20×10^7	3.78×10^2	4.85×10^2	0.73	7.29×10^7	0.28
15	20	0.3	30	1.33	1.05	15.07	19.9	1.83×10^8	3.94×10^2	4.69×10^2	0.74	7.27×10^7	0.30
15	20	0.3	100	1.39	1.09	14.36	20.9	5.13×10^8	4.03×10^2	4.53×10^2	0.76	7.25×10^7	0.30

Table A4. Numerical results with shallow stiffening ($\gamma = 0.4$, $\theta_0 = 20$, and $H^* > 7$)

θ_0	H^*	h^*	$\Delta\eta$	T_{\max}^*	$\langle T^* \rangle$	Nu	θ	Ra_i	v_{rms}^*	v_s^*	$P_{0,1}$	Φ	Φ_δ/Φ
20	8	0.1	3	1.06	0.74	7.52	21.3	3.80×10^6	5.14×10^1	7.50×10^1	0.51	2.58×10^7	0.34
20	8	0.1	10	1.08	0.74	7.42	21.6	5.10×10^6	5.77×10^1	9.57×10^1	0.50	2.57×10^7	0.37
20	8	0.1	30	1.09	0.75	7.32	21.9	7.02×10^6	5.60×10^1	9.39×10^1	0.49	2.56×10^7	0.38
20	8	0.1	100	1.12	0.76	7.11	22.5	1.37×10^7	5.59×10^1	8.57×10^1	0.52	2.52×10^7	0.38
20	8	0.2	3	1.10	0.75	7.28	22.0	7.94×10^6	5.74×10^1	9.07×10^1	0.47	2.57×10^7	0.37
20	8	0.2	10	1.13	0.78	7.08	22.6	1.52×10^7	5.34×10^1	7.60×10^1	0.50	2.57×10^7	0.34
20	8	0.2	30	1.14	0.81	7.02	22.8	1.89×10^7	7.63×10^1	9.28×10^1	0.63	2.53×10^7	0.33
20	8	0.3	3	1.10	0.76	7.29	22.0	7.81×10^6	5.88×10^1	9.37×10^1	0.48	2.57×10^7	0.37
20	8	0.3	10	1.13	0.80	7.06	22.7	1.62×10^7	6.88×10^1	9.41×10^1	0.53	2.54×10^7	0.36
20	8	0.3	30	1.15	0.85	6.95	23.0	2.42×10^7	1.17×10^2	1.30×10^2	0.62	2.48×10^7	0.36
20	8	0.3	100	1.20	0.90	6.69	23.9	6.19×10^7	1.32×10^2	1.24×10^2	0.65	2.45×10^7	0.34
20	12	0.1	3	1.12	0.82	10.74	22.4	1.18×10^7	1.50×10^2	2.32×10^2	0.65	4.12×10^7	0.26
20	12	0.1	10	1.13	0.84	10.65	22.5	1.44×10^7	1.77×10^2	2.58×10^2	0.69	4.08×10^7	0.27
20	12	0.1	30	1.14	0.86	10.56	22.7	1.75×10^7	2.01×10^2	2.72×10^2	0.72	4.02×10^7	0.28
20	12	0.1	100	1.15	0.89	10.42	23.1	2.47×10^7	2.03×10^2	2.48×10^2	0.74	3.97×10^7	0.29
20	12	0.2	3	1.14	0.86	10.54	22.8	1.85×10^7	2.05×10^2	2.86×10^2	0.70	4.09×10^7	0.27
20	12	0.2	10	1.17	0.89	10.30	23.3	3.22×10^7	2.23×10^2	2.86×10^2	0.72	4.05×10^7	0.29
20	12	0.2	30	1.19	0.92	10.08	23.8	5.51×10^7	2.33×10^2	2.68×10^2	0.75	4.03×10^7	0.32
20	12	0.3	3	1.15	0.86	10.43	23.0	2.36×10^7	1.96×10^2	2.74×10^2	0.69	4.09×10^7	0.28
20	12	0.3	10	1.18	0.90	10.18	23.6	4.26×10^7	2.05×10^2	2.57×10^2	0.71	4.06×10^7	0.29
20	12	0.3	30	1.21	0.93	9.91	24.2	8.38×10^7	2.13×10^2	2.46×10^2	0.71	4.03×10^7	0.31
20	12	0.3	100	1.25	0.96	9.59	25.0	1.94×10^8	2.19×10^2	2.30×10^2	0.71	3.94×10^7	0.33
20	16	0.1	3	1.17	0.89	13.73	23.3	3.22×10^7	3.15×10^2	4.66×10^2	0.73	5.66×10^7	0.25
20	16	0.1	10	1.17	0.91	13.64	23.5	3.79×10^7	3.22×10^2	4.48×10^2	0.75	5.61×10^7	0.26
20	16	0.1	30	1.18	0.92	13.54	23.6	4.52×10^7	3.27×10^2	4.28×10^2	0.75	5.55×10^7	0.28
20	16	0.1	100	1.21	0.95	13.19	24.3	8.75×10^7	3.38×10^2	4.03×10^2	0.78	5.50×10^7	0.29
20	16	0.2	3	1.18	0.91	13.52	23.7	4.69×10^7	3.31×10^2	4.62×10^2	0.72	5.66×10^7	0.26
20	16	0.2	10	1.22	0.95	13.18	24.3	8.98×10^7	3.47×10^2	4.38×10^2	0.74	5.61×10^7	0.29
20	16	0.2	30	1.25	0.98	12.81	25.0	1.87×10^8	3.64×10^2	4.34×10^2	0.74	5.58×10^7	0.31
20	16	0.2	100	1.29	1.02	12.41	25.8	4.24×10^8	3.82×10^2	3.94×10^2	0.73	5.55×10^7	0.34
20	16	0.3	3	1.19	0.92	13.46	23.8	5.27×10^7	3.15×10^2	4.38×10^2	0.72	5.64×10^7	0.26
20	16	0.3	10	1.23	0.96	13.00	24.6	1.26×10^8	3.23×10^2	4.01×10^2	0.74	5.60×10^7	0.28
20	16	0.3	30	1.27	0.99	12.60	25.4	2.89×10^8	3.32×10^2	3.80×10^2	0.75	5.58×10^7	0.30
20	16	0.3	100	1.31	1.02	12.23	26.2	6.45×10^8	3.34×10^2	3.47×10^2	0.75	5.55×10^7	0.32
20	20	0.1	3	1.21	0.95	16.54	24.2	8.04×10^7	4.53×10^2	6.49×10^2	0.75	7.23×10^7	0.27
20	20	0.1	10	1.22	0.96	16.37	24.5	1.05×10^8	4.65×10^2	6.32×10^2	0.77	7.18×10^7	0.28
20	20	0.1	100	1.29	1.01	15.48	25.9	4.59×10^8	4.89×10^2	6.44×10^2	0.82	7.06×10^7	0.27
20	20	0.2	3	1.23	0.96	16.30	24.6	1.17×10^8	4.66×10^2	6.42×10^2	0.74	7.22×10^7	0.28
20	20	0.2	10	1.26	0.99	15.88	25.2	2.31×10^8	4.70×10^2	5.94×10^2	0.74	7.19×10^7	0.30
20	20	0.2	30	1.30	1.02	15.42	26.0	5.07×10^8	4.90×10^2	5.88×10^2	0.74	7.17×10^7	0.31
20	20	0.2	100	1.35	1.06	14.88	26.9	1.34×10^9	5.16×10^2	5.64×10^2	0.74	7.13×10^7	0.31
20	20	0.3	3	1.23	0.97	16.25	24.6	1.28×10^8	4.44×10^2	6.03×10^2	0.74	7.22×10^7	0.28
20	20	0.3	10	1.28	1.00	15.68	25.5	3.27×10^8	4.45×10^2	5.51×10^2	0.76	7.18×10^7	0.29
20	20	0.3	100	1.36	1.06	14.78	27.1	1.65×10^9	4.59×10^2	4.78×10^2	0.76	7.13×10^7	0.33

Table A5. Numerical results with shallow stiffening ($\gamma = 0.4$, $\theta_0 = 25$, and $H^* > 7$)

θ_0	H^*	h^*	$\Delta\eta$	T_{\max}^*	$\langle T^* \rangle$	Nu	θ	Ra_i	v_{rms}^*	v_s^*	$P_{0.1}$	Φ	Φ_δ/Φ
25	8	0.1	3	1.09	0.76	7.37	27.1	9.32×10^6	6.88×10^1	1.07×10^2	0.49	2.46×10^7	0.36
25	8	0.1	10	1.29	1.16	6.20	32.3	1.86×10^9	2.99×10^3	6.71×10^{-4}	0.00	2.05×10^7	0.43
25	8	0.1	30	1.29	1.16	6.22	32.2	1.67×10^9	3.02×10^3	9.93×10^{-5}	0.00	2.06×10^7	0.43
25	8	0.1	100	1.11	0.80	7.20	27.8	1.87×10^7	8.04×10^1	9.53×10^1	0.55	2.40×10^7	0.34
25	8	0.2	3	1.11	0.77	7.22	27.7	1.69×10^7	6.59×10^1	9.62×10^1	0.49	2.48×10^7	0.36
25	8	0.2	10	1.14	0.80	7.00	28.6	4.12×10^7	7.04×10^1	9.08×10^1	0.54	2.45×10^7	0.35
25	8	0.2	30	1.20	0.86	6.66	30.0	1.84×10^8	1.00×10^2	6.78×10^1	0.47	2.47×10^7	0.32
25	8	0.2	100	1.20	0.88	6.70	29.9	1.60×10^8	1.62×10^2	8.69×10^1	0.66	2.35×10^7	0.32
25	8	0.3	3	1.10	0.78	7.25	27.6	1.46×10^7	6.60×10^1	9.81×10^1	0.49	2.46×10^7	0.36
25	12	0.1	3	1.13	0.84	10.60	28.3	3.10×10^7	1.42×10^2	2.11×10^2	0.62	3.93×10^7	0.28
25	12	0.1	10	1.14	0.85	10.50	28.6	4.14×10^7	1.60×10^2	2.19×10^2	0.66	3.88×10^7	0.28
25	12	0.1	30	1.16	0.89	10.34	29.0	6.60×10^7	2.09×10^2	2.34×10^2	0.72	3.80×10^7	0.28
25	12	0.3	3	1.15	0.86	10.42	28.8	5.22×10^7	1.72×10^2	2.28×10^2	0.66	3.90×10^7	0.28
25	12	0.3	10	1.18	0.90	10.14	29.6	1.20×10^8	2.12×10^2	2.42×10^2	0.70	3.79×10^7	0.31
25	16	0.1	30	1.22	0.95	13.09	30.6	3.33×10^8	3.71×10^2	4.17×10^2	0.76	5.42×10^7	0.28
25	16	0.2	3	1.19	0.93	13.41	29.8	1.52×10^8	3.62×10^2	4.41×10^2	0.74	5.32×10^7	0.28
25	16	0.2	10	1.22	0.96	13.12	30.5	3.08×10^8	3.86×10^2	4.11×10^2	0.74	5.72×10^7	0.29
25	16	0.3	10	1.23	0.96	13.04	30.7	3.72×10^8	6.10×10^2	4.00×10^2	0.76	7.53×10^7	0.37
25	20	0.1	3	1.22	0.96	16.35	30.6	3.38×10^8	5.04×10^2	6.82×10^2	0.76	6.81×10^7	0.27
25	20	0.1	10	1.25	0.97	15.96	31.4	7.30×10^8	5.22×10^2	7.03×10^2	0.78	6.79×10^7	0.27
25	20	0.1	30	1.30	0.97	15.33	32.6	2.64×10^9	4.88×10^2	7.25×10^2	0.77	7.06×10^7	0.22
25	20	0.1	100	1.35	1.06	14.77	33.9	9.60×10^9	1.28×10^3	6.47×10^2	0.80	6.99×10^7	0.21

Table A6. Numerical results with shallow stiffening ($\gamma = 0.4$, $\theta_0 = 15$, and $H^* < 7$)

θ_0	H^*	h^*	$\Delta\eta$	T_{\max}^*	$\langle T^* \rangle$	Nu	θ	Ra_i	v_{rms}^*	v_s^*	$P_{0.1}$	Φ	Φ_δ/Φ
15	2	0.1	3	0.82	0.51	2.44	12.3	5.59×10^4	7.67×10^0	5.19×10^0	0.15	2.44×10^6	0.88
15	2	0.1	10	0.82	0.51	2.44	12.3	5.59×10^4	7.67×10^0	5.18×10^0	0.20	2.44×10^6	0.88
15	2	0.1	30	0.82	0.51	2.44	12.3	5.59×10^4	7.67×10^0	5.17×10^0	0.25	2.44×10^6	0.88
15	2	0.1	100	0.82	0.51	2.44	12.3	5.59×10^4	7.67×10^0	5.19×10^0	0.27	2.44×10^6	0.88
15	2	0.2	3	0.83	0.52	2.41	12.4	6.44×10^4	7.88×10^0	4.85×10^0	0.35	2.42×10^6	0.88
15	2	0.2	10	0.84	0.52	2.38	12.6	7.50×10^4	8.17×10^0	4.80×10^0	0.35	2.54×10^6	0.88
15	2	0.2	30	0.84	0.52	2.38	12.6	7.70×10^4	8.20×10^0	4.75×10^0	0.45	2.54×10^6	0.87
15	2	0.2	100	0.84	0.52	2.38	12.6	7.74×10^4	8.21×10^0	4.74×10^0	0.52	2.55×10^6	0.87
15	2	0.3	3	0.85	0.52	2.36	12.7	8.78×10^4	8.27×10^0	4.55×10^0	0.38	2.50×10^6	0.87
15	2	0.3	10	0.86	0.54	2.31	13.0	1.13×10^5	8.76×10^0	3.94×10^0	0.46	2.36×10^6	0.89
15	2	0.3	30	0.91	0.63	2.19	13.7	2.54×10^5	1.18×10^1	4.22×10^{-3}	0.00	1.17×10^6	0.87
15	2	0.3	100	0.91	0.63	2.19	13.7	2.55×10^5	1.18×10^1	1.24×10^{-3}	0.00	1.16×10^6	0.87
15	4	0.1	3	0.90	0.60	4.42	13.6	2.16×10^5	2.28×10^1	2.60×10^1	0.50	1.07×10^7	0.52
15	4	0.1	10	0.91	0.60	4.42	13.6	2.19×10^5	2.28×10^1	2.59×10^1	0.45	1.07×10^7	0.52
15	4	0.1	30	0.91	0.60	4.40	13.6	2.34×10^5	2.28×10^1	2.59×10^1	0.54	1.07×10^7	0.52
15	4	0.1	100	0.91	0.60	4.40	13.7	2.36×10^5	2.28×10^1	2.59×10^1	0.55	1.07×10^7	0.51
15	4	0.2	3	0.91	0.61	4.38	13.7	2.49×10^5	2.26×10^1	2.50×10^1	0.48	1.07×10^7	0.49
15	4	0.2	10	0.95	0.62	4.23	14.2	4.22×10^5	2.58×10^1	2.98×10^1	0.44	1.05×10^7	0.52
15	4	0.2	30	0.94	0.63	4.23	14.2	4.12×10^5	2.54×10^1	2.53×10^1	0.70	1.05×10^7	0.48
15	4	0.2	100	0.95	0.64	4.19	14.3	4.85×10^5	2.58×10^1	2.45×10^1	0.71	1.05×10^7	0.48
15	4	0.3	3	0.92	0.62	4.33	13.9	2.95×10^5	2.28×10^1	2.35×10^1	0.46	1.06×10^7	0.48
15	4	0.3	10	0.94	0.65	4.24	14.2	4.09×10^5	2.33×10^1	2.12×10^1	0.65	1.05×10^7	0.46
15	4	0.3	30	0.96	0.67	4.17	14.4	5.25×10^5	2.41×10^1	1.99×10^1	0.55	1.04×10^7	0.46
15	4	0.3	100	0.99	0.69	4.06	14.8	8.02×10^5	2.62×10^1	2.05×10^1	0.54	1.02×10^7	0.49
15	6	0.1	3	0.99	0.67	6.07	14.8	8.22×10^5	3.67×10^1	5.24×10^1	0.62	1.86×10^7	0.39
15	6	0.1	10	0.99	0.68	6.05	14.9	8.74×10^5	3.65×10^1	5.15×10^1	0.65	1.86×10^7	0.38
15	6	0.1	30	0.99	0.68	6.04	14.9	9.09×10^5	3.64×10^1	5.08×10^1	0.67	1.86×10^7	0.38
15	6	0.1	100	1.02	0.68	5.89	15.3	1.34×10^6	3.91×10^1	5.51×10^1	0.60	1.85×10^7	0.40
15	6	0.2	3	1.00	0.69	6.02	15.0	9.50×10^5	3.66×10^1	4.95×10^1	0.66	1.86×10^7	0.36
15	6	0.2	10	1.03	0.71	5.80	15.5	1.73×10^6	4.14×10^1	5.46×10^1	0.71	1.84×10^7	0.35
15	6	0.2	30	1.06	0.74	5.65	15.9	2.72×10^6	4.60×10^1	5.43×10^1	0.75	1.83×10^7	0.33
15	6	0.2	100	1.10	0.77	5.45	16.5	5.06×10^6	5.91×10^1	6.26×10^1	0.82	1.80×10^7	0.35
15	6	0.3	3	1.01	0.70	5.93	15.2	1.21×10^6	3.65×10^1	4.78×10^1	0.66	1.85×10^7	0.37
15	6	0.3	10	1.08	0.76	5.57	16.2	3.40×10^6	4.68×10^1	5.33×10^1	0.59	1.81×10^7	0.39
15	6	0.3	30	1.11	0.80	5.39	16.7	6.03×10^6	7.22×10^1	7.49×10^1	0.63	1.78×10^7	0.40
15	6	0.3	100	1.16	0.84	5.18	17.4	1.24×10^7	7.88×10^1	6.61×10^1	0.68	1.76×10^7	0.36

Table A7. Numerical results with shallow stiffening ($\gamma = 0.4$, $\theta_0 = 20$ & 25 , and $H^* < 7$)

θ_0	H^*	h^*	$\Delta\eta$	T_{\max}^*	$\langle T^* \rangle$	Nu	θ	Ra_i	v_{rms}^*	v_s^*	$P_{0.1}$	Φ	Φ_δ/Φ
20	2	0.1	3	0.96	0.65	2.08	19.3	4.62×10^5	9.88×10^0	2.53×10^{-3}	0.00	7.02×10^5	0.94
20	2	0.2	3	0.96	0.65	2.08	19.3	4.62×10^5	9.89×10^0	1.02×10^{-3}	0.00	7.02×10^5	0.94
20	2	0.3	3	0.96	0.65	2.08	19.3	4.66×10^5	9.90×10^0	8.63×10^{-4}	0.00	6.98×10^5	0.94
20	4	0.1	3	1.01	0.66	3.97	20.2	1.18×10^6	2.28×10^1	2.09×10^1	0.56	9.79×10^6	0.58
20	4	0.1	10	0.98	0.64	4.07	19.7	7.25×10^5	2.21×10^1	4.45×10^1	0.37	9.86×10^6	0.53
20	4	0.1	30	1.01	0.67	3.94	20.3	1.35×10^6	2.33×10^1	2.03×10^1	0.58	9.66×10^6	0.57
20	4	0.1	100	1.02	0.67	3.93	20.4	1.45×10^6	2.35×10^1	2.08×10^1	0.50	9.59×10^6	0.56
20	4	0.2	3	1.00	0.66	3.99	20.1	1.09×10^6	2.62×10^1	4.06×10^1	0.43	9.70×10^6	0.52
20	4	0.2	10	1.02	0.67	3.93	20.4	1.46×10^6	2.57×10^1	3.53×10^1	0.53	9.70×10^6	0.50
20	4	0.2	30	1.04	0.69	3.83	20.9	2.56×10^6	2.47×10^1	2.05×10^1	0.49	9.70×10^6	0.54
20	4	0.2	100	1.05	0.69	3.81	21.0	2.86×10^6	2.67×10^1	2.63×10^1	0.50	9.57×10^6	0.53
20	4	0.3	3	1.03	0.69	3.89	20.6	1.82×10^6	2.38×10^1	1.87×10^1	0.58	9.74×10^6	0.51
20	4	0.3	10	1.21	0.99	3.31	24.1	7.64×10^7	3.69×10^2	9.90×10^{-7}	0.00	6.30×10^6	0.60
20	6	0.1	3	1.05	0.71	5.73	20.9	2.66×10^6	3.78×10^1	4.56×10^1	0.49	1.78×10^7	0.41
20	6	0.1	10	1.04	0.70	5.78	20.8	2.28×10^6	3.73×10^1	5.86×10^1	0.45	1.78×10^7	0.43
20	6	0.1	30	1.07	0.72	5.63	21.3	3.99×10^6	3.48×10^1	4.54×10^1	0.52	1.77×10^7	0.40
20	6	0.1	100	1.08	0.72	5.58	21.5	4.85×10^6	3.58×10^1	5.00×10^1	0.46	1.76×10^7	0.43
20	6	0.2	3	1.06	0.71	5.65	21.2	3.66×10^6	3.35×10^1	4.62×10^1	0.46	1.78×10^7	0.42
20	6	0.2	10	1.09	0.73	5.51	21.8	6.55×10^6	3.72×10^1	4.73×10^1	0.53	1.77×10^7	0.42
20	6	0.2	30	1.09	0.74	5.51	21.8	6.36×10^6	4.24×10^1	5.40×10^1	0.62	1.76×10^7	0.41
20	6	0.2	100	1.13	0.78	5.31	22.6	1.51×10^7	4.90×10^1	4.60×10^1	0.68	1.74×10^7	0.37
20	6	0.3	3	1.07	0.72	5.63	21.3	3.93×10^6	3.78×10^1	5.60×10^1	0.42	1.77×10^7	0.46
20	6	0.3	10	1.11	0.76	5.42	22.1	9.33×10^6	3.96×10^1	4.84×10^1	0.45	1.76×10^7	0.42
20	6	0.3	30	1.14	0.79	5.27	22.8	1.80×10^7	4.60×10^1	4.96×10^1	0.57	1.74×10^7	0.37
20	6	0.3	100	1.43	1.21	4.20	28.6	7.48×10^9	3.65×10^3	1.97×10^{-8}	0.00	8.70×10^6	0.53
25	2	0.1	3	0.98	0.66	2.04	24.6	6.29×10^5	7.35×10^0	5.99×10^{-8}	0.00	3.93×10^5	0.96
25	2	0.2	3	0.98	0.66	2.04	24.6	6.29×10^5	7.35×10^0	5.48×10^{-8}	0.00	3.93×10^5	0.96
25	2	0.3	3	0.98	0.66	2.04	24.6	6.29×10^5	7.36×10^0	5.06×10^{-8}	0.00	3.93×10^5	0.96
25	4	0.1	3	1.17	0.97	3.41	29.3	8.56×10^7	3.90×10^2	8.75×10^{-6}	0.00	6.68×10^6	0.60
25	4	0.2	3	1.17	0.97	3.41	29.3	8.59×10^7	3.90×10^2	4.69×10^{-6}	0.00	6.66×10^6	0.60
25	4	0.3	3	1.19	0.98	3.36	29.7	1.33×10^8	4.66×10^2	4.88×10^{-8}	0.00	6.40×10^6	0.60
25	6	0.1	3	1.25	1.09	4.80	31.2	6.39×10^8	1.39×10^3	1.79×10^{-4}	0.00	1.36×10^7	0.49
25	6	0.2	3	1.25	1.09	4.79	31.3	7.05×10^8	1.23×10^3	2.44×10^{-5}	0.00	1.33×10^7	0.46
25	6	0.3	3	1.28	1.12	4.67	32.1	1.56×10^9	2.00×10^3	3.59×10^{-4}	0.00	1.31×10^7	0.50

Table A8. Numerical results with shallow stiffening ($\gamma = 0.8$)

θ_0	H^*	h^*	$\Delta\eta$	T_{\max}^*	$\langle T^* \rangle$	Nu	θ	Ra_i	v_{rms}^*	v_s^*	$P_{0.1}$	Φ	Φ_δ/Φ
10	2	0.2	1000	0.85	0.58	2.35	8.5	1.91×10^5	1.79×10^1	3.66×10^{-2}	0.00	2.07×10^6	0.86
10	2	0.3	10	0.80	0.53	2.50	8.0	1.07×10^5	1.37×10^1	3.83×10^0	0.46	2.72×10^6	0.83
10	2	0.3	100	0.88	0.60	2.27	8.8	2.66×10^5	1.89×10^1	1.23×10^{-1}	0.00	1.75×10^6	0.87
10	3	0.2	10	0.75	0.52	3.98	7.5	6.49×10^4	2.01×10^1	1.77×10^1	0.66	7.61×10^6	0.63
10	3	0.2	100	1.00	0.78	2.99	10.0	1.03×10^6	5.80×10^1	4.43×10^{-2}	0.00	4.41×10^6	0.68
10	3	0.3	10	0.83	0.58	3.62	8.3	1.49×10^5	2.14×10^1	1.39×10^1	0.57	6.95×10^6	0.70
10	4	0.1	10	0.77	0.55	5.18	7.7	7.89×10^4	2.89×10^1	3.37×10^1	0.73	1.17×10^7	0.53
10	4	0.1	100	0.78	0.55	5.15	7.8	8.36×10^4	2.90×10^1	3.34×10^1	0.79	1.17×10^7	0.54
10	4	0.1	1000	0.78	0.55	5.15	7.8	8.38×10^4	2.90×10^1	3.33×10^1	0.79	1.17×10^7	0.54
10	4	0.2	10	0.82	0.59	4.90	8.2	1.31×10^5	3.11×10^1	3.14×10^1	0.59	1.14×10^7	0.58
10	4	0.2	100	1.11	0.92	3.61	11.1	3.26×10^6	1.13×10^2	7.14×10^{-3}	0.00	7.34×10^6	0.61
10	4	0.3	10	0.88	0.63	4.52	8.8	2.80×10^5	3.55×10^1	3.27×10^1	0.53	1.09×10^7	0.64
12	2	0.2	10	0.80	0.51	2.49	9.6	7.47×10^4	1.05×10^1	4.58×10^0	0.57	2.80×10^6	0.85
12	2	0.2	100	0.90	0.60	2.23	10.7	2.55×10^5	1.58×10^1	3.23×10^{-1}	0.00	1.70×10^6	0.91
12	2	0.3	10	0.90	0.61	2.22	10.8	2.79×10^5	1.59×10^1	6.30×10^{-1}	0.00	1.63×10^6	0.91
12	2	0.3	100	0.92	0.62	2.18	11.0	3.34×10^5	1.68×10^1	4.51×10^{-2}	0.00	1.46×10^6	0.93
12	3	0.1	10	0.82	0.54	3.68	9.8	8.91×10^4	1.79×10^1	1.57×10^1	0.48	7.11×10^6	0.67
12	3	0.1	100	0.82	0.54	3.67	9.8	9.03×10^4	1.79×10^1	1.56×10^1	0.52	7.12×10^6	0.67
12	3	0.1	1000	0.82	0.54	3.67	9.8	9.04×10^4	1.79×10^1	1.56×10^1	0.54	7.13×10^6	0.67
12	3	0.2	10	0.84	0.57	3.57	10.1	1.24×10^5	1.84×10^1	1.36×10^1	0.69	6.95×10^6	0.67
12	3	0.2	100	0.87	0.60	3.46	10.4	1.78×10^5	2.00×10^1	1.18×10^1	0.67	6.66×10^6	0.70
12	3	0.2	1000	0.89	0.62	3.38	10.6	2.30×10^5	2.14×10^1	1.08×10^1	0.76	6.48×10^6	0.72
12	4	0.1	10	0.86	0.60	4.65	10.3	1.61×10^5	2.56×10^1	2.64×10^1	0.66	1.11×10^7	0.57
12	4	0.1	100	0.86	0.60	4.63	10.4	1.67×10^5	2.56×10^1	2.61×10^1	0.78	1.11×10^7	0.57
12	4	0.1	1000	0.87	0.60	4.61	10.4	1.78×10^5	2.56×10^1	2.62×10^1	0.76	1.11×10^7	0.57
12	4	0.2	10	0.88	0.63	4.53	10.6	2.15×10^5	2.61×10^1	2.39×10^1	0.63	1.09×10^7	0.57
12	4	0.2	100	0.91	0.66	4.38	11.0	3.20×10^5	2.75×10^1	2.14×10^1	0.65	1.06×10^7	0.62
12	4	0.2	1000	1.13	0.93	3.53	13.6	5.50×10^6	1.33×10^2	1.59×10^{-4}	0.00	7.12×10^6	0.61
12	4	0.3	10	0.93	0.67	4.31	11.1	3.96×10^5	2.72×10^1	2.17×10^1	0.56	1.05×10^7	0.66
14	2	0.1	10	0.86	0.55	2.34	12.0	1.13×10^5	9.86×10^0	3.49×10^0	0.35	2.23×10^6	0.90
14	2	0.1	100	0.86	0.55	2.34	12.0	1.13×10^5	9.85×10^0	3.49×10^0	0.36	2.23×10^6	0.90
14	2	0.1	1000	0.86	0.55	2.34	12.0	1.13×10^5	9.85×10^0	3.49×10^0	0.36	2.23×10^6	0.90
14	2	0.2	10	0.91	0.59	2.21	12.7	2.42×10^5	1.25×10^1	2.32×10^0	0.57	1.73×10^6	0.93
14	2	0.2	100	0.89	0.62	2.24	12.5	2.02×10^5	1.20×10^1	1.17×10^{-3}	0.00	1.36×10^6	0.85
14	2	0.3	10	0.90	0.62	2.22	12.6	2.26×10^5	1.24×10^1	7.89×10^{-3}	0.00	1.28×10^6	0.84
14	3	0.1	10	0.89	0.60	3.36	12.5	2.03×10^5	1.79×10^1	1.21×10^1	0.51	6.46×10^6	0.71
14	3	0.1	100	0.89	0.60	3.35	12.5	2.04×10^5	1.79×10^1	1.21×10^1	0.54	6.46×10^6	0.71
14	3	0.1	1000	0.89	0.60	3.35	12.5	2.05×10^5	1.80×10^1	1.20×10^1	0.53	6.47×10^6	0.71
14	3	0.2	10	0.91	0.62	3.28	12.8	2.72×10^5	1.91×10^1	1.07×10^1	0.61	6.29×10^6	0.70
14	3	0.3	100	1.08	0.84	2.79	15.1	3.13×10^6	7.22×10^1	3.55×10^{-4}	0.00	3.59×10^6	0.70
14	4	0.1	10	0.94	0.65	4.27	13.1	3.91×10^5	2.49×10^1	2.17×10^1	0.63	1.05×10^7	0.60
14	4	0.1	100	0.94	0.65	4.26	13.2	4.05×10^5	2.49×10^1	2.29×10^1	0.48	1.05×10^7	0.60
14	4	0.1	1000	0.98	0.67	4.10	13.7	6.98×10^5	3.11×10^1	2.52×10^1	0.58	1.02×10^7	0.61
14	4	0.2	10	0.95	0.67	4.20	13.3	4.90×10^5	2.55×10^1	2.02×10^1	0.66	1.04×10^7	0.59
14	4	0.2	100	1.04	0.74	3.86	14.5	1.74×10^6	4.71×10^1	2.13×10^1	0.78	9.60×10^6	0.58
14	4	0.2	1000	1.11	0.79	3.59	15.6	5.46×10^6	8.42×10^1	3.14×10^1	0.84	9.15×10^6	0.58